

# Scaling and tuning to criticality in resting-state human magnetoencephalography

Irem Topal,<sup>1</sup> Anna Poggialini,<sup>1</sup> Marco Dal Maschio,<sup>1</sup> Daniele De Martino,<sup>2</sup> Oren Shriki,<sup>3</sup> and Fabrizio Lombardi<sup>1,\*</sup>

<sup>1</sup>*Department of Biomedical Sciences, University of Padova, Padova, Italy*

<sup>2</sup>*Biofisika Institute (CSIC,UPV-EHU) and Ikerbasque Foundation, Bilbao 48013, Spain*

<sup>3</sup>*Department of Industrial Engineering and Management,*

*School of Brain Sciences and Cognition, Ben-Gurion University of the Negev, Beer-Sheva, Israel*

(Dated: March 17, 2026)

From  $1/f$  noise to neuronal avalanches, evidence of scaling in brain activity has been increasingly linked to tuning to or near criticality. The concept of scaling is intimately related to the renormalization group (RG), in essence providing coarse-grained, simplified descriptions that generalize to classes of diverse physical systems. Following the RG idea, scaling laws have been reported in populations of spiking neurons at microscopic scales. Whether similar scaling principles govern large-scale neural activity in the human brain and how they relate to underlying neural physiology remain unresolved. Here, we analyze large-scale electrophysiological recordings (MEG) of human resting-state brain activity and apply a RG-inspired coarse-graining approach to track collective neural dynamics across spatial scales. We find that multiple observables exhibit robust scale-invariant behavior under coarse-graining: activity variance and correlations grow according to power laws, covariance eigen-spectra follow a characteristic scaling relation, and neuronal avalanche statistics remain invariant. Using an analytically tractable neural network model, we show that the observed scaling signatures arise when the system operates slightly below criticality, and that the scaling exponents depend on the excitation–inhibition balance. These findings demonstrate that RG-inspired scaling analysis can uncover signatures of critical dynamics in non-invasive human electrophysiology and suggest a principled route toward estimating excitation–inhibition balance from large-scale brain recordings.

## I. INTRODUCTION

Criticality has emerged in recent years as an effective framework for quantifying the internal state of the brain [1–4]. The idea that the brain may operate near a phase transition dates back to the early 1950’s and originates from the analogy between collective behaviors in neural populations and (inanimate) physical systems—in particular, ferromagnets—at criticality [5], a special point of the parameter space separating an ordered from a disordered phase. Intuitively, one would link the emergence of collective/cooperative behaviors to the presence of numerous direct interactions among the many components of a system. However, stunning collective properties emerge at criticality even in systems with local, short range interactions [6], above all scale invariance (or simply scaling) and long-range power-law correlations.

So, what are we expected to observe, practically, if a population of neurons operated at criticality? The recent advancement in neural recording techniques has allowed simultaneous tracking of an ever increasing number of neurons, prompting a renewed interest in brain criticality. Observations of neuronal avalanches across scales, systems, and species have provided important evidence of power-law, scale-invariant features in collective neural activity [7–12]. Similarly, long-range spatio-temporal correlations have been reported in brain activity, in particular in humans and rats [13–21]. All of these could be considered hints of criticality that arise from tracking spatio-temporal, collective neural dynamics [22–24]. On

the other hand, focusing on strictly static or equilibrium (thermodynamic) aspects, evidence of tuning to criticality has come from maximum entropy models of neuronal populations [25–27]. In this context, signatures of criticality are given by extrema in thermodynamic quantities of the data-inferred model, such as maxima in the susceptibility and in the specific heat [6, 28].

Those hallmarks of criticality boil down to one key fact, i.e. the dynamics are independent of the microscopic details. This implies that, at criticality, most degrees of freedom are irrelevant to obtain an essential understanding (or model) of the system, and opens the way for simplified descriptions in terms of coarse-grained variables integrating out ‘irrelevant details’. This idea is formalized in the renormalization group (RG) of equilibrium statistical physics [29]. Intuitively, one initially deals with many variables—these could be binary neurons—which define the microscopic scale of the system under scrutiny. Imagine now performing a ‘local’ coarse-graining by averaging over small neighborhoods in space, or more generally, by replacing a group of local units with a single representative variable—which needs to be chosen appropriately [30]. As one iterates such a process, the joint distribution of coarse-grained variables evolves and in most cases becomes simpler, as fast fluctuations are averaged out. Under the assumption of the RG, the resulting coarse-grained, macroscopic description should be more general than the underlying microscopic structures and form a universality class, where the observables are described by scaling functions and power laws with a set of critical exponents that are common to many (microscopically) diverse systems and ultimately depend solely on general features such as symmetries

\* [fabrizio.lombardi@at.unipd.it](mailto:fabrizio.lombardi@at.unipd.it)

and dimensionality [6]. A major obstacle in applying RG ideas to neural data lies in the fact that, unlike most physical systems, the underlying interaction structure is highly complex—including the morphology of individual neurons—and remains largely unknown.

A simplification in the spirit of the RG has recently been proposed for populations of real neurons in the hippocampus [31]. In this approach, spatial coarse-graining of local variables is replaced by a correlation-based coarse-graining of individual neurons. This choice is motivated by the extended, non-local nature of neurons, which also make long-range synaptic connections. Since in systems with local interactions microscopic variables are most strongly correlated with (spatial) nearest neighbors, correlation is used in this approach as a proxy for neighborhood. To guide intuition, suppose that we start with a population of  $N$  neurons. We quantify the correlations between all possible couples of neurons, and then ‘couple’ each neuron with its most correlated neuron by summing their respective activity at each time interval. In doing so, we create  $N/2$  new time series, which we generically refer to as ‘variables’. The process can be iterated until we are left with a single variable. Conceptually, this procedure is identical to the block-renormalization, or spatial averaging, first proposed by Kadanoff on regular lattices [30]. In [31], it was shown that under iterated coarse-graining, the activity of a network of hippocampal neurons approached a fixed non-Gaussian distribution, and several quantities, e.g. correlation time, showed a non-trivial power-law scaling as a function of the coarse-graining level. These properties signal that the system is near a non-trivial fixed point of the RG, i.e. criticality [31]

Similar results have been found in population of neurons from different regions of the mouse cortex [32, 33] and, to some extent, in Blood Oxygenation Level Dependent (BOLD) signals [34]. However, such evidence of criticality has not been confirmed in electrophysiological recordings of large-scale human brain activity to date. Here, we aim to close this gap by investigating scaling behaviors of magneto-encephalography (MEG) recordings of the awake resting-state under coarse-graining, and verify that collective brain dynamics, e.g. neuronal avalanches, are invariant under the same coarse-graining procedure—a key prediction of the renormalization group for systems at criticality. M/EEG signals result (mostly) from ionic currents to which large populations of neurons contribute [35, 36], and can be considered in turn as an effective coarse-grained measure of the underlying neural activity. Hence, finding scaling laws in the MEG as those reported for populations of spiking neurons would significantly extend the range of validity of previous observations at small spatial scales, and represent a comprehensive evidence of tuning to criticality in the brain, linking renormalization, neuronal avalanches, long-range correlations.

## II. RESULTS

### A. Resting-state MEG obeys scaling laws indicative of criticality

We analyze MEG during 4 minutes of eyes-closed resting-state in 100 healthy subjects (Appendix A). We normalize MEG signals to zero mean and unit standard deviation (SD) and identify positive and negative extremes of signal fluctuations greater than a threshold  $e = \pm 3\text{SD}$  (Appendix A). We refer to them as extreme events or simply events, and in our analysis they will be the equivalent of spikes in populations of neurons [31]. This preprocessing maps continuous signals to discrete time series of number of events and ensures that coarse-graining is performed on the same time series that are used to define neuronal avalanches in the MEG [9, 18].

We illustrate the coarse-graining procedure in Fig. 1. For pedagogical purposes, we start with  $N = 4$  MEG signals from sensors in the frontal and parietal areas (F46, F56, P44 and P45, Fig. 1, left). For each signal, we show the corresponding extreme events at the bottom (colored bars). The initial step of the procedure is labeled  $k = 0$  (original, non coarse-grained signals). Then, the sequence of events from each sensor is summed with the sequence of events of its most correlated sensor, leading to  $N_k = N/K = N/2^k$  new variables in step  $k = 1$  (Fig. 1, middle). The new variables are then normalized in such a way that the average number of events in non-empty time bins is one, as in the initial step  $k = 0$  (Appendix B). The procedure continues until  $N_k = 1$ , i.e., when only a single variable is left (Fig. 1, right). Throughout the paper,  $k$  will indicate the coarse-graining step,  $K = 2^k$  the number of signals iteratively summed up to step  $k$ , and  $N_k = N/K$  the number of variables at each step  $k$ . Hence, the variables in step  $k$  are clusters of size  $K$  and are labeled as  $x_i^{(K)}$  ( $i = 1, \dots, N_k$ ).

To implement this procedure on MEG recordings, at each step  $k$ , we calculate the correlation matrix  $C_{ij}^k$  among the  $N_k$  variables and uniquely couple them according to its entries, as illustrated in Fig. 1 and detailed in Appendix B. At each step  $k$ , we first analyze two basic quantities: the distribution of activity,  $Q_K(x)$ , and the probability of silence  $P_0(K)$  across the  $N_k$  variables (Appendix B). We find that the distribution of activity rapidly approaches a non-Gaussian, exponential-like fixed form for increasing values of the cluster size  $K$  (Fig. 2A). This is in agreement with previous observations in populations of spiking neurons [31, 32], and indicates that brain activity is close to a non-Gaussian fixed point of the renormalization group, namely the statistics of the activity is independent of the scale of observation (coarse-graining). We note that for weakly dependent or independent variables coarse-graining would lead to a fixed Gaussian distribution. Similarly, for a collection of independent variables the probability of silence,  $P_0(K)$ , decays exponentially with  $K$  [31]. In contrast, we find that in resting-state activity the probability of silence

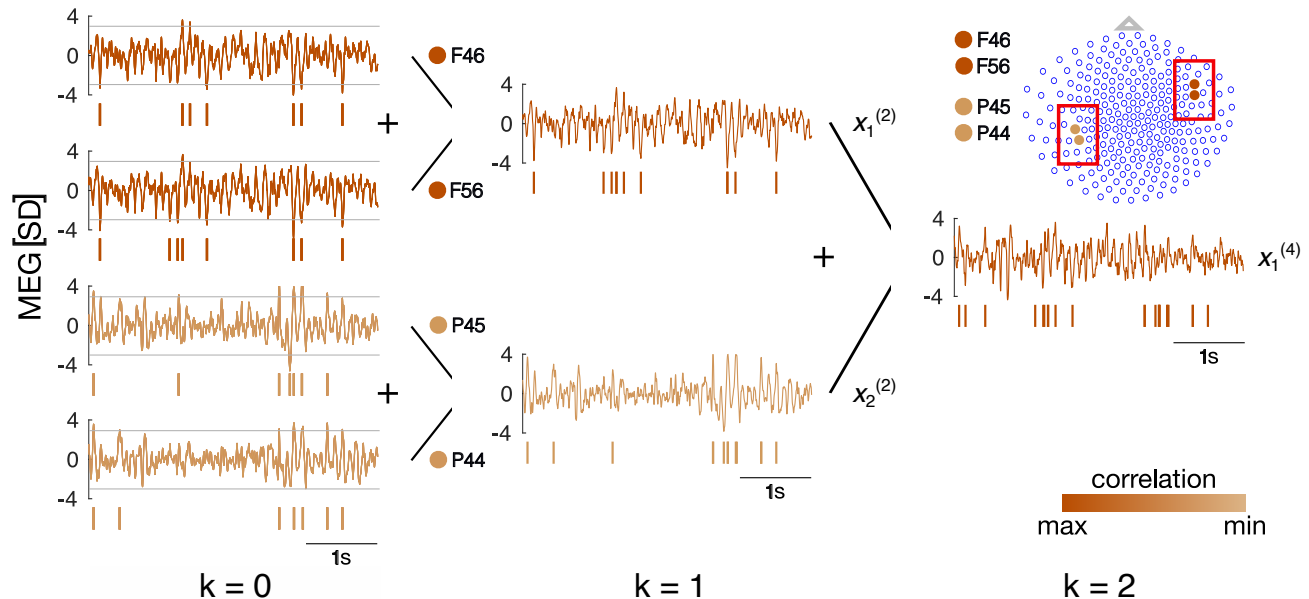


FIG. 1. **Phenomenological Renormalization Group analysis of MEG data.** Schematic presentation of the coarse-graining procedure for four MEG sensors. Sensor signals ( $z$ -normalized, amplitude in unit of standard deviation (SD); see Appendix A) are initially binarized by marking as 1's the extremes of positive and negative excursions beyond a threshold  $e = \pm 3$  SD (horizontal gray lines) and as 0's all other points (**left**). Resulting binary time series (colored bars) are shown at the bottom of each signal, where vertical lines represent tips of above-threshold excursions, which we refer to as extreme events. The case  $k = 0$  corresponds to the original MEG signals (left). Signals are sorted in couples, from the most to the least correlated. The first couple is made by the sensors F46 and F56 (dark red dots), the second by the sensors P45 and P44 (light red dots). Location of these sensors on the scalp is shown on the right upper corner. At each step  $k$  of the coarse-graining, pairwise correlations between sensor time series are calculated. Each sensor is paired with its most correlated sensor, and their activity is summed and results in a new time-series (**middle**,  $k = 1$ ). On top of each time series of events we show the signal resulting from summing together the original sensor (or variable) signals, which is the continuous,  $z$ -normalized coarse-grained variable. The resulting summed activity defines the *coarse-grained variables*. At each successive iteration of the procedure, we compute the correlations between coarse-grained variables and group the most correlated pairs by summing their activity. This process is repeated iteratively until only one variable is left (**right**,  $k = 2$ ).

decays as a stretched exponential,  $P_0(K) \propto \exp(-aK^\beta)$ , with  $\beta = 0.82 \pm 0.02$  (mean  $\pm$  SD; Fig. 2B, individual subject; Fig. S1B, average over  $n = 100$  subjects), in close agreement with previous reports for populations of spiking neurons [31–33]. These behaviors are consistent across subjects (see Supplementary Materials, Fig. S1, for the average over  $n = 100$  subjects) and very robust with respect to binarization threshold and temporal binning (Figs. S2-S4).

To understand whether this fixed point of resting-state brain activity is consistent with criticality, we next iteratively analyzed cluster dynamics as a function of  $K$ . Since our coarse-graining procedure simply consists in iteratively summing an increasing number of signals, the mean activity scales linearly with  $K$  (see Appendix B). For independent variables, we also expect the variance to scale linearly with  $K$ , since the covariance between variables is zero. In the opposite scenario of a collection of fully correlated variables, the variance scales instead as  $\text{Var}(K) \propto K^2$  (Appendix B). We find that resting-state activity falls between these two limiting

cases (Fig. 2C). In fact, we observe that the variance of the non-normalized cluster activity scales as a power-law of  $K$ ,  $\text{Var}(K) \propto K^\alpha$ , with  $\alpha = 1.32 \pm 0.03$  (mean  $\pm$  SD;  $n = 100$ ). This ‘intermediate’ value is close to previous observations in populations of neurons [31–33], and indicates a self-similar structure of the underlying correlations associated to a non-trivial growth of the activity variance—reminiscent of criticality, a non-trivial fixed point of the RG. The scaling of activity variance is robust and weakly dependent on the binarization threshold and temporal binning used in the analysis, as demonstrated by the analysis over all subjects (Figs. S1) and in a range of thresholds and time bins (Figs. S3-S4).

If we are near criticality, then we expect that the correlations scale with the cluster size  $K$ , as we include more and more sensors, i.e. an increasing portion of the system. Specifically, this implies that the autocorrelation time of the variables,  $\tau_c$ , increases with  $K$  as a power-law, i.e.  $\tau_c(K) \propto K^z$ . To test whether this scaling holds in resting-state brain activity, we first evaluated the average autocorrelation for each cluster of size  $K$ ,  $C_K(\tau)$

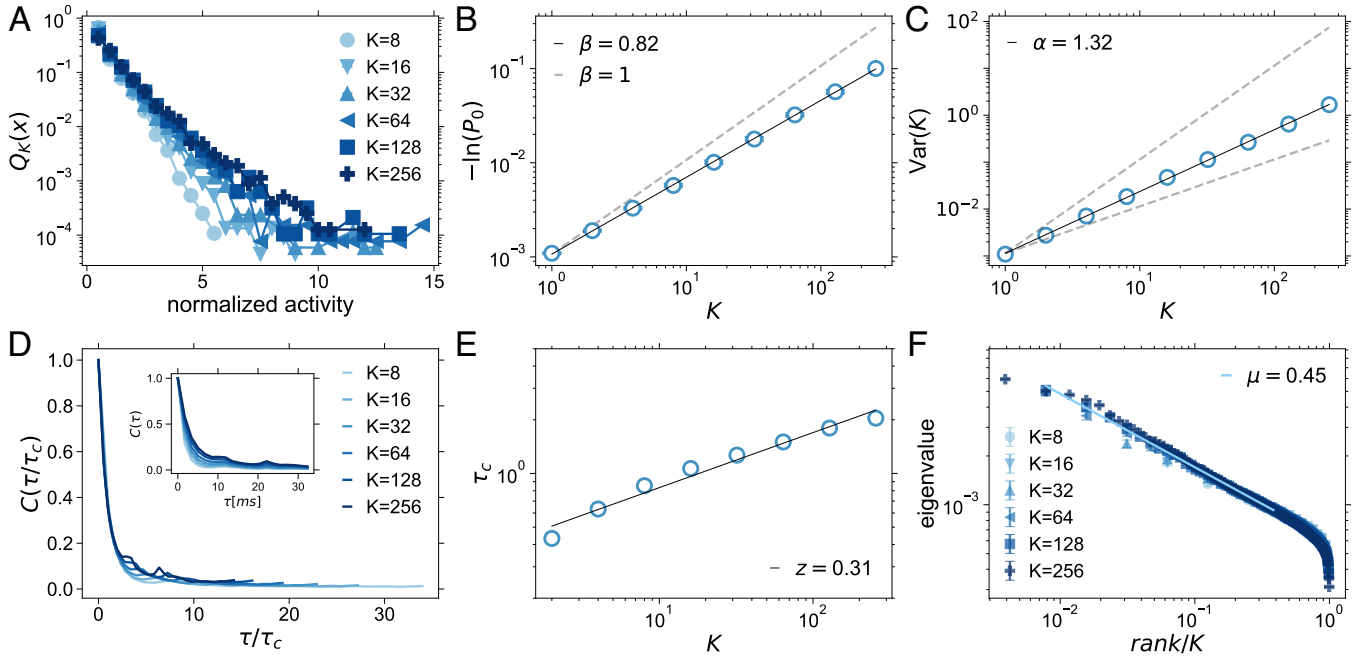


FIG. 2. **Scaling in resting-state human MEG.** **A.** Probability distribution of normalized non-zero activity for the cluster sizes  $K \geq 8$ . Darker blue = Increasing cluster size. **B.** The log-probability of silence in coarse-grained variables ( $\ln P_0$ ) as a function of cluster size ( $K$ ). The solid black line represents a linear least-squares fit of  $-\ln P_0 = bK^\beta$  in log-log scale, where  $\beta = 0.82$  ( $R^2 = 0.99$ ,  $p < 10^{-5}$ ). The gray dashed line indicates the prediction for independent variables. For each  $K$ , SEM is calculated across coarse-grained variables. Error bars are always smaller than the marker size. **C.** Variance ( $\text{Var}$ ) of the non-normalized coarse-grained variables as a function of the cluster size,  $K$ . The solid black line corresponds to the linear least-square fit,  $\log \text{Var}(K) = \alpha \cdot \log K + b$ , where  $\alpha = 1.32$  ( $R^2 = 0.99$ ,  $p < 10^{-5}$ ). gray dashed lines indicate reference growth rates: bottom, linear scaling ( $\alpha = 1$ ) characteristic of independent variables; top, quadratic scaling ( $\alpha = 2$ ) expected for fully correlated variables. **D.** Average correlation functions for different cluster sizes,  $K$ , collapse on a single curve after rescaling time,  $\tau$ , by the auto-correlation time  $\tau_c$ . Inset: Original autocorrelation for different  $K$ . **E.** The autocorrelation time,  $\tau_c$ , as a function of  $K$ , grows as  $\tau_c \propto K^z$ . The solid black line corresponds to the linear least-square fit,  $\log \tau_c(K) = z \cdot \log K + b$ , where  $z = 0.31$  ( $R^2 = 0.97$ ,  $p < 10^{-5}$ ). **F.** Eigenvalues of covariance matrices within clusters of different sizes. Larger clusters correspond to darker colors. The solid line is a linear least squares fit to  $\log \lambda = \log b(\text{rank}/K)^{-\mu}$  performed for  $K = 128$ . The fitting range is  $[2/128, 50/128]$ . The analysis is performed on an individual subject using  $e = \pm 3\text{SD}$  and  $\delta = 1T_s = 1.67$  ms, where  $T_s$  is the sampling time (Appendix A).

(Appendix B). We observe that the autocorrelation depends on  $K$  (Fig. 2D, inset), and its decay becomes slower as  $K$  increases. However, when we rescale the time by the autocorrelation time  $\tau_c$  calculated at each  $K$ , all different curves collapse onto the same functional form (Fig. 2D). Importantly, we find that  $\tau_c$  depends on  $K$  according to a power-law with exponent  $z = 0.33 \pm 0.03$  (mean  $\pm$  SD; Fig. 2E, individual subject). The analysis over all subjects shows that the scaling of  $\tau_c$  is robust (see Supplementary Materials, Fig. S1), and is stable with respect to temporal binning and binarization thresholds (Figs. S3-S4). We note that  $\tau_c$  tend to decrease with increasing threshold values, in particular for  $K > 64$ . This behavior must be ascribed to the increasing sparsity of time series induced by higher thresholds, which likely weakens the correlations present in the original data.

Next, we look inside the clusters of size  $K$  and analyze their covariance matrix. If correlations are self-similar, as our analysis suggests, then the eigenvalues of the covariance matrix should obey a power-law relation with

their respective ranks, independently of  $K$  (Appendix B). This requirement is condensed in Eq. B6, stating that the eigenspectrum of the covariance matrix, i.e.  $\lambda(\text{rank})$ , has the same form when ranks are rescaled by the cluster size  $K$ . As a consequence, plotting  $\lambda$  as a function of  $\text{rank}/K$  should result in a collapse of all eigenspectra for different  $K$  on the same power-law with exponent  $\mu$ . This prediction is robustly satisfied by resting-state brain activity. In Fig. 2F, we show the eigenspectra of the covariance matrix for different  $K$  in an individual subject. They all collapse on a single power-law,  $\lambda \propto (\text{rank}/K)^{-\mu}$ , with  $\mu = 0.45$ . Eigenspectra before rescaling ranks are shown in Fig. S5 of the Supplementary Materials (SM). The scaling of  $\lambda(\text{rank})$  shows little variability across subjects (Fig. S1F;  $\mu = 0.41 \pm 0.03$ ; mean  $\pm$  SD;  $n = 100$ ), and in a range of thresholds (Fig. S3) and bin sizes (Fig. S4;  $2T_s \leq \delta \leq 5T_s$ , with  $T_s$  the sampling time).

We then asked whether there is any empirical relationship between scaling exponents characterizing the MEG of the resting-state. For example, for independent vari-

ables we know that the exponent  $\beta$  controlling the scaling of  $P_0$  with  $K$  must tend to one, and so the exponent  $\alpha$  for the variance of cluster activity. When correlations increase, instead,  $\beta$  is expected to decrease and  $\alpha$  to increase. Thus, we can anticipate that  $\beta$  and  $\alpha$  should be anti-correlated. Plotting  $\alpha$  versus  $\beta$  for all subjects (Fig. 3A), we find that  $\beta$  decreases linearly with  $\alpha$ , i.e.  $\beta = -0.54 \cdot \alpha + 1.53$ . Additionally, we observe that the value of the exponent  $\alpha$  correlates with the scaling exponent of the eigenspectrum of the covariance matrix (Fig. 3B):  $\mu = 0.61 \cdot \alpha - 0.39$ . This relationship indicates that  $\mu \rightarrow 0$  (no scaling) for uncorrelated variables, and increases linearly with  $\alpha$  over the range of non-trivial values measured in resting-state activity (Fig. 3B). Due to the relation between  $\alpha$  and  $\beta$ , the exponent  $\mu$  must in turn be correlated with  $\beta$ , as we found (Fig. 3C;  $\mu = -1.0 \cdot \beta + 1.24$ ). Next, we consider the largest eigenvalue,  $\lambda_1$ , of the covariance matrix and measure how it scales with  $K$ . We observe that  $\lambda_1(K) \sim K^\epsilon$ , and that the exponent  $\epsilon$  is related to the exponent  $\alpha$  as  $\epsilon \approx \alpha - 1$ , as shown in [37] (Fig. 3D). Specifically, we find  $\epsilon = 1.46\alpha - 1.54$ . However, outliers analysis shows that the linear regression between  $\alpha$  and  $\epsilon$  is strongly influenced by certain subjects [38]. When removing those subjects, we obtain  $\epsilon = 1.09\alpha - 1.07$  ( $R^2 = 0.53$ ,  $p < 10^{-5}$ ;  $n = 91$ ; errors on the fit parameters estimated via bootstrap: 0.04 and 0.05, respectively), very close to theoretical prediction [37].

Taken together, the non-Gaussian form of the distributions of activity and the scaling behaviors observed in all analyzed quantities indicate that MEG resting-state dynamics is at a non-Gaussian fixed point of the phenomenological renormalization group (PRG). To support this evidence, we performed three different tests. First, we performed the analysis on MEG signals with randomized phases (Appendix D). Phase randomization preserves autocorrelation of individual signals while destroying cross-correlations among signals. PRG analysis on phase-randomized data (Fig. S6) shows a Gaussian distribution of activity—activity that is also strongly suppressed—, trivial scaling for the probability of silence ( $\beta = 1.000 \pm 0.001$ ) and for the variance ( $\alpha = 0.990 \pm 0.001$ ), and no scaling in the correlation time  $\tau_c$  ( $z \approx 0$ ), with fast decaying autocorrelation independent of  $K$  (Fig. S6D-E). As for the eigenspectra, we observe absence of clear scaling compared with original data (Fig. S6F), with the exception of a short regime for high rank eigenvalues. Furthermore, the relationship between  $\alpha$  ( $\beta$ ) and  $\epsilon$  is not satisfied (see SM, Fig. S7).

Second, we scramble signal amplitudes in such a way to destroy the autocorrelation of individual signals while preserving their cross-correlations (trace randomization; see Appendix D). In this case, all analyzed quantities behave as for original data, except for the autocorrelation of variables, which becomes weaker and does not scale with  $K$  (Fig. S8). This indicates that autocorrelation of individual signals influences the scaling of  $\tau_c$ , while all other quantities depend mainly on the collective correla-

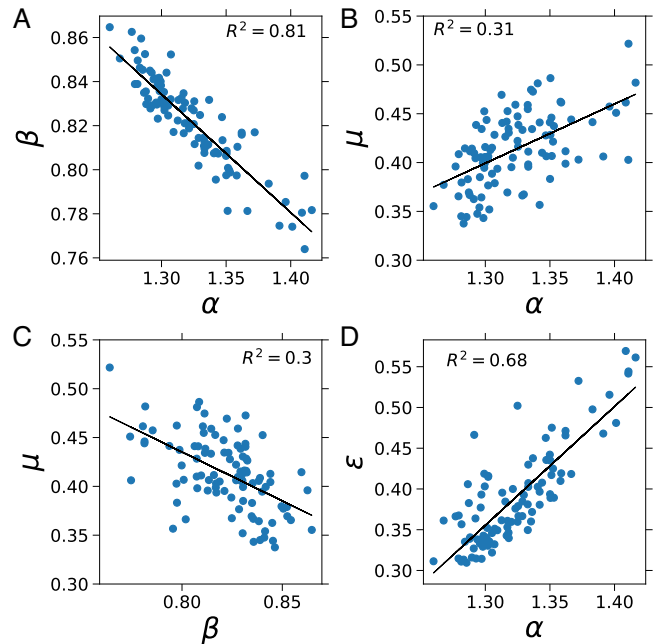


**FIG. 3. Relationships between scaling exponents in the MEG of the resting state.** **A.** The scaling exponent of the cluster variance is inversely proportional to the exponent  $\beta$  that characterizes the probability of silence  $P_0(K)$ , i.e.  $\beta = -0.54\alpha + 1.53$  (linear least square fit:  $R^2 = 0.81$ ,  $p < 10^{-5}$ ;  $n = 98$ . Two subjects were excluded based on Cook’s distance [38]). **B.** The exponent  $\mu$  characterizing the eigenvalue spectrum of the covariance matrix increases linearly with  $\alpha$ :  $\mu = 0.61\alpha - 0.39$  (linear least square fit:  $R^2 = 0.31$ ,  $p < 10^{-5}$ ;  $n = 98$ ). **C.** As expected from A and B, the exponent  $\mu$  decreases for increasing values of  $\beta$ . The relationship between  $\mu$  and  $\beta$  is well described by a linear equation,  $\mu = -1.0\beta + 1.24$  (linear least square fit:  $R^2 = 0.3$ ,  $p < 10^{-5}$ ;  $n = 98$ ). **D.** The scaling exponent of the largest eigenvalue of the covariance matrix,  $\epsilon$ , increases for increasing values of  $\alpha$ , as shown by the linear relationship  $\epsilon = 1.46\alpha - 1.54$  (linear least square fit:  $R^2 = 0.68$ ,  $p < 10^{-5}$ ;  $n = 98$ ).

tion structure.

Third, we keep the signals unchanged but pair variables randomly throughout all steps of the procedure (random coarse-graining; Appendix D). In this case, we observe both deviations from scaling and, in particular, from data collapse in comparison to original data (Fig. S9). The distributions of cluster activity tend to stay non-Gaussian, but they are not consistent over coarse-graining steps and seem not to converge to a fixed functional form, although we cannot exclude it for  $K \rightarrow \infty$ —because of the limited number of sensors. Deviations from scaling occur at large cluster sizes,  $K > 64$ , in  $-\ln P_0$  and in the variance (Fig. S9B, C). Concerning the eigenspectra of the covariance matrices, we observe clear deviations from the data collapse compared to the original coarse-graining procedure, although the eigenspectra still follow power-law behaviors (Fig. S9F). This implies a  $K$ -dependent exponents  $\mu$ .

Surrogate tests indicate that, altogether, robust scaling behaviors and data collapses in resting-state MEG result from the intrinsic structure of the underlying correlations. Random coarse-graining might not fully destroy the scaling features of the original data because correlations among MEG sensors are non-negligible over large areas, i.e. they are non-local and decay rather slowly with distance [9]. Summing the activity of most correlated sensors to generate coarse-grained variables is equivalent to grouping nearest neighbors in systems with local interactions (Fig. 1), as in the block renormalization technique [30]. If correlations were strictly local, random coarse-graining would produce the same effects of phase randomization (Fig. S6). However, since in the MEG sensor array correlations are rather long-range, the effect of random pairing becomes apparent only when the full structure of the correlations kicks in: (i) in the co-activation of sensors, implied in  $Q_K(x)$ , (ii) in the scaling of cluster activity at large cluster sizes  $K$ , (iii) in the scaling of the eigenspectrum of the covariance matrix, which depends on  $K$  and breaks down at low ranks (long wavelength).

Before turning our attention to dynamics of neuronal avalanches under coarse-graining, we discuss the effect of the variable normalization and signal discretization choice on the non-Gaussian distributions and scaling behaviors of resting-state brain activity. We have shown that the results presented in Fig. 2 are robust in a wide range of thresholds (Fig. S2-S3). We only considered threshold  $e > 2.7$  SD, where the distribution of signal amplitudes deviates from a Gaussian [9] (see Appendix A), and took both positive ( $x > +e$ ) and negative extremes ( $x < -e$ ). First, we notice that results are stable when considering only positive or only negative extremes (SM, Table I). If we lower the binarization threshold to progressively include an increasing number of signal points (and noise), we observe that the distribution of activity tends to a Gaussian for increasing  $K$  (Fig. S10). However, scaling is preserved in the probability of silence, activity variance, and (partially) in the eigenspectra, but not in the autocorrelation time (Fig. S10). In the limit of continuous signals (variables), we observe that the distribution of activity deviates from a Gaussian and shows long tails (positive and negative) before coarse-graining and for a number of coarse-graining steps (Fig. S11)—nearly independently of  $K$ —and converges to its Gaussian core for large  $K$ . At the same time, we observe no scaling in the silence probability and in the autocorrelation time, while the variance tends to scale with  $K$  as in fully correlated variables, i.e.  $\alpha \approx 2$  and the eigenspectrum of the covariance matrix shows limited scaling (also dependent on  $K$ ) (Fig. S11).

An alternative to selecting only extremes of the above-threshold excursions is represented by taking all points belonging to them. Also in this case, we found robust, fixed non-Gaussian distribution of activity and non-trivial scaling in all analyzed quantities (Fig. S12), al-

though with different exponents (see SM, Table II-III for a comparison between the two methods). However, the relations between scaling exponents are similar to those we found when considering extreme events only (compare Fig. S13 with Fig. 3). We note that in this case scaling behaviors tend to be well preserved for low discretization threshold ( $e = 0.5$ SD), i.e. when more Gaussian noise is included (Fig. S14).

Finally, we note that repeating the analysis on non-normalized variables—i.e. without normalizing variables at each step  $k$  as explained in Methods B—provides comparable results (Fig. S15).

## B. Scaling of neuronal avalanches is invariant under coarse-graining

The coarse-graining analysis suggests that resting-state brain activity is close to a fixed point of the dynamics characterized by scale invariance, i.e. criticality. Prior evidence of brain tuning to criticality in resting MEG was provided by scaling of neuronal avalanches and long-range temporal correlations [9, 18, 24]. Here we ask how neuronal avalanche dynamics evolve under the coarse-graining procedure studied above, and show that they are invariant.

In Fig. 4A, we show the evolution of neuronal avalanches over five coarse-graining steps, from  $K = 2$  to  $K = 16$ . The upper row,  $K = 1$ , corresponds to the raster plot with avalanches obtained from the original MEG signals. Neuronal avalanches are labeled as  $A_i$  and defined as sequences of time bins continuously populated with at least one extreme event (blue dots) on any of the MEG sensors or variables (Appendix C). As we proceed with coarse-graining, we notice that the number of variables decreases, as well as the number of extreme events (blue dots), whereas the time windows occupied by the avalanches (i.e. the durations) remain unchanged (Fig. 4A). To quantify the dynamics of avalanches across coarse-graining steps, we plot the distributions of avalanche sizes and durations as a function of  $K$  (Fig. 4B). We observe that the largest avalanche size decreases as  $K$  increases (Fig. 4B, top). However, the scaling regime of the distribution (approximately two decades) remains nearly unchanged and is followed by an exponential cutoff whose onset in turn depends on  $K$ . This suggests that the distribution of avalanche sizes for different  $K$  follows the scaling form  $P(s) = s^{-\tau} f(s/K^\zeta)$ , where  $\tau_s$  is the power-law exponent and  $f(s/K^\zeta)$  a scaling function, the exponent  $\zeta$  capturing the dependence of the exponential cutoff on  $K$ . By plotting  $s_s^\tau P(s)$  versus  $s/K^\zeta$ , we found that distributions of avalanche sizes for different cluster sizes,  $K$ , collapse onto a single curve, confirming that the finite-size scaling ansatz,  $P(s) = s^{-\tau} f(s/K^\zeta)$ , is valid (Fig. S14). This indicates that the scaling regime of  $P(s)$  is stable across coarse-graining steps.

Similarly, the scaling behavior of the duration distribu-

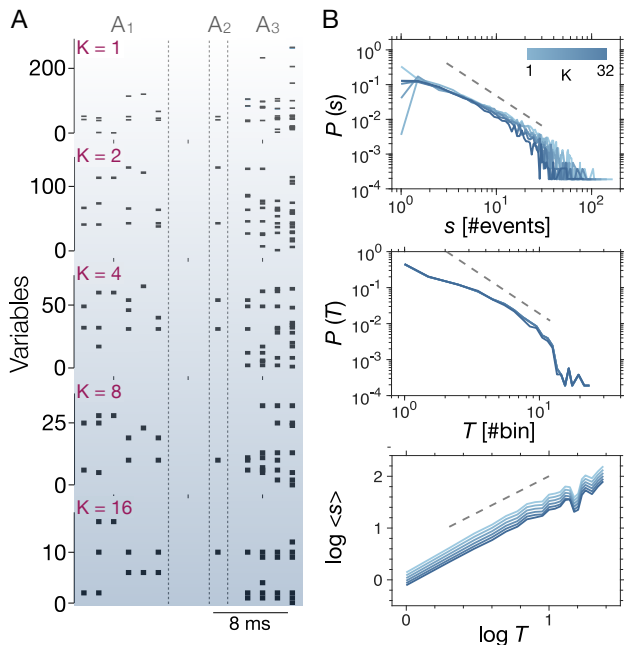


FIG. 4. **Invariant avalanche scaling under PRG.** Evolution of neuronal avalanches under PRG (left). At each PRG step, a reduced set of coarse-grained variables are obtained, from the initial 273 sensors ( $K = 1$ , top) to 17 variables for  $K = 16$  (bottom). Neuronal avalanches are defined as consecutive sequences of events across sensors in time bins (delimited by dashed lines), bounded by periods with no events. Avalanche size  $s$  is defined as the number of events (blue dots) across all sensors during the lifetime of the avalanche; duration  $T$  is the number of consecutive time bins belonging to the avalanche times the bin size. The distribution of avalanche sizes,  $P(S)$ , and avalanche durations,  $P(T)$ , do not change over consecutive steps of the PRG (right top and middle). Moreover, the scaling relation between  $s$  and  $T$  is also invariant under coarse-graining (right, bottom). The analysis is performed using  $e = \pm 3\text{SD}$  and  $\delta = 1T_s = 1.67$  ms, with  $T_s$  the sampling time (Appendix A).

tion is independent of  $K$  (Fig. 4B, middle and Fig. S17). Importantly, we find that coarse-graining also preserves the scaling relation between avalanche sizes and durations,  $\langle s \rangle \propto T^\gamma$ , with the exponent  $\gamma$  remaining nearly unchanged over coarse-graining steps (Fig. 4B, bottom and Fig. S17). Because the number of variables progressively decreases as  $K$  increases, the cutoff of the power-law regime shifts towards smaller  $s$ . In contrast, durations are almost unaffected by coarse-graining, i.e. the temporal localization of avalanches is nearly fixed. As a consequence,  $\langle s \rangle(T)$  is vertically shifted, but its scaling behavior remains stable (Fig. 4B, bottom). Maximum likelihood estimates of  $\tau_s$  show a slight increase with  $K$ , which is likely due to the increasing weight of the tail on the fit for larger  $K$  (Fig. S17). On the other hand,  $\gamma$  and the avalanche duration exponent,  $\alpha_t$ , remained nearly unchanged (Fig. S17).

### C. Excitation/inhibition balance modulates scaling exponents near criticality

To understand the emergence of scaling in resting-state brain activity in relation to neural dynamics and criticality, we simulated resting-state activity using a recently proposed interpretable neural network model [39]. This model has a genuine non-equilibrium critical point, and reproduces both local, individual sensor dynamics—including neural oscillations—and collective scale-free neuronal avalanches. Importantly, its analytical tractability enables us to make direct contact with MEG data, and infer its two free parameters (Appendix E).

The model consists of a population of  $N$  interacting neurons whose dynamics is self-regulated by a time-varying feedback that depends on the ongoing population activity level. Neurons are all excitatory, and are simulated as binary units  $s_i = \pm 1$  ( $i = 1, 2, \dots, N$ , with  $N = 273 \cdot 10^3$ , unless specified differently) that are active when  $s_i = +1$  or inactive when  $s_i = -1$ . Here we consider the simplest, fully homogeneous scenario in which neurons interact with each other through synapses of equal strength  $J_{ij} = J = 1$  (see Appendix E for details). The ongoing network activity is defined as  $m(t) = \frac{1}{N} \sum_{i=1}^N s_i(t)$ , and each neuron experiences a uniform negative feedback,  $h$ , that depends on  $m$  as  $\dot{h} = -cm$ , with  $c$  a positive constant. The negative feedback can be identified with inhibitory drives from the neuronal population that affect individual neurons with a delay given by the characteristic time  $1/c$ . Neurons  $s_i$  are stochastically activated according to the Glauber dynamics, where the new state of the neuron  $s_i$  is drawn from the marginal Boltzmann-Gibbs distribution  $P(s_i) \propto \exp(\beta_T \tilde{h}_i s_i)$ , with  $\tilde{h}_i = \sum_{j \neq i} J_{ij} s_j + h$ , where  $\beta_T$  is a parameter reminiscent of the inverse temperature for an Ising model. For our simulations, we consider an all-to-all network connectivity, i.e.  $J_{ij} = 1, \forall i, j$  and  $i \neq j$ . Network behavior is determined by the two parameters  $c$  and  $\beta_T$ , which control feedback strength and proximity to criticality, respectively. For  $c > 0$ , the model is driven out of equilibrium and has a critical point at  $\beta_T = \beta_c = 1$  [39, 40]. Slightly below the critical point, the model exhibits both neuronal avalanches and oscillations characteristics of the MEG signals [39].

To estimate the parameters  $\beta_T$  and  $c$ , we fit the analytical form of the model autocorrelation to the MEG signal autocorrelation (Appendix E). Parameters inferred across all sensors and subjects suggested baseline values of  $\beta_T = 0.99$  and  $c = 0.01$  [39], which we use for all subsequent data-model comparisons. To make contact with the data, we parcel our simulated network into  $M = 273$  equally-sized disjoint subsystems of  $n_{\text{sub}} = N/M = 1000$  neurons each, and consider each subsystem activity  $m_\mu$ ,  $\mu = 1, \dots, M$ , as the equivalent of a single MEG sensor signal. All quantities for the model then follow the same definition as for the data, allowing us to perform direct side-by-side comparisons with data (Appendix E). We

use the same threshold value  $e = 3.0$  SD for both data and model analyses (Appendix E). Extensive robustness analyses confirm that model behaviors are stable in a range of thresholds (Figs. S18), and we detail them one by one in the following.

We find that the inferred model closely reproduces resting-state activity under coarse-graining. First, the distribution of activity,  $Q_K(x)$ , tends to a non-Gaussian fixed form for increasing cluster size  $K$  (Fig. 5A), and the probability of silence scales non-trivially with  $K$ , i.e.  $P_0(K) = e^{-aK^\beta}$ , with  $\beta \approx 0.8$  in agreement with the empirical value (Fig. 5B). Similarly, and in line with the relation between exponents found in empirical data, the activity variance grows as a power-law with  $K$ , with an exponent  $\alpha \approx 1.3$ , as observed in real data (Fig. 5C). In both the data and the model, we observe that temporal correlations scale with the cluster size (Fig. 5D), and the auto-correlation time,  $\tau_c$ , increases as a power-law, with an exponent  $z \approx 0.3$  (Fig. 5E). Turning to the eigenspectrum of the covariance matrix, the model shows a scaling regime with an exponent  $\mu \approx 0.3$ , which is approximately independent of the cluster size  $K$ , in agreement with the prediction  $\lambda \propto (\text{rank}/K)^{-\mu}$  (Fig. 5F). We note that  $\alpha$  and  $z$  are close but slightly larger than the corresponding empirical values ( $z$ :  $0.382 \pm 0.002$  vs.  $0.33 \pm 0.03$ ;  $\alpha$ :  $1.385 \pm 0.010$  vs  $1.32 \pm 0.03$ ), while  $\mu$  is smaller ( $\mu$ :  $0.265 \pm 0.005$  vs  $0.41 \pm 0.03$ ). Scaling behaviors show little variability—mostly around the largest cluster size—for bin sizes  $2dt \leq \delta \leq 5dt$ , where  $dt$  is the simulation time and corresponds to a system sweep of Monte Carlo updates (Fig. S19).

The inferred model is very close to its critical point. A longstanding question about the emergence of collective behaviors in brain activity concerns the dynamical regime in which they can all coexist [41, 42]. Is this a localized or an extended region of the parameter's space? If, as our empirical results suggest, this dynamical regime corresponds to criticality, how close to it does one need to be in order to observe scaling in cluster activity? And how do exponents depend on the distance to criticality?

To address this question, we investigate the behavior of the model for increasing distance to criticality, defined as  $\text{DTC} = \beta_c - \beta_T$ . We find that both the distribution of activity and the scaling of all analyzed quantities depend on DTC, and are non-trivial in a (rather) small DTC range (Fig. 6, Figs. S20-S23). In Fig. 6A, we show the distribution of activity in clusters of size  $K = 256$  for a range of DTC (see Fig. S20 for other cluster sizes). We observe that the distribution of activity remains stable and non-Gaussian in a narrow range of DTC comprised between 0.01 and 0.03. The distribution becomes increasingly sensitive to DTC and rapidly approaches a Gaussian behavior for  $\text{DTC} > 0.05$  (Fig. 6A). Similarly, the exponents  $\beta$  and  $\alpha$  rapidly approach one as DTC increases, and are equal to one for  $\text{DTC} = 0.1$  (Fig. 6 and Fig. S21). In parallel, the autocorrelation of the variables drops drastically for  $\text{DTC} > 0.03$  and becomes nearly in-

dependent of the cluster  $K$  for  $\text{DTC} > 0.05$ , i.e.  $z \approx 0$  (Fig. 6, Fig. S21, S22). Further, the eigenspectrum of the covariance matrix shows power-law scaling on a narrow range of DTC (Fig. S23), with  $0.2 \lesssim \mu \lesssim 0.3$  approaching zero (flat eigenspectrum) for  $\text{DTC} \gtrsim 0.1$  (Fig. 6). These results suggest that one needs to stay rather close to criticality to observe the non-trivial scaling behaviors of resting-state MEG.

Next, we investigate the role of the feedback,  $h$ , by turning it off, i.e. by setting  $c = 0$ , while keeping the network very close to criticality ( $\beta_T = 0.99$ ,  $\text{DTC} = 0.01$ ) (Fig. S24). Absence of negative feedback effectively makes the network fully excitatory and thus mimics an unbalanced E/I ratio, which has been linked to modulation of scaling in the activity power spectrum [43]. In this scenario, we simultaneously observe a sharp increase in the exponent  $\beta$ , which approaches one ( $\beta = 0.94$ , Fig. S24B), and a sharp decrease in the exponent  $\alpha$  for the activity variance, which also approaches one ( $\alpha = 1.15$ ). In parallel, we find no scaling of  $\tau_c$  and eigenspectra of the cluster covariance matrices, which are nearly constant (Fig. S24E, F).

Overall, this indicates that feedback plays an important role in reproducing the scaling behaviors of resting-state brain activity in humans. In its simplest configuration, the feedback represents an inhibitory drive that influences neurons on a certain time scale controlled by  $c$  (Appendix E). Absence of feedback mimics a scenario without inhibition, where neural dynamics is solely controlled by excitatory neuronal interactions ( $J_{ij}$ ). The opposite scenario, i.e. neural activity driven only by feedback (and noise), is obtained by setting  $J_{ij} = 0$ , e.g. non-interacting neurons. In this case, the distribution of activity approaches a Gaussian, and all other quantities show trivial or no scaling (Fig. S25).

Before summarizing our findings, a word of caution is needed to avoid misinterpretation of the approach we have taken here. In equilibrium critical phenomena, critical exponents have precise values and are well defined at the critical point of the phase transition,  $\beta_T = \beta_c$  [6]. The RG allows one to obtain theoretical values of the critical exponents as well as the scaling relationships among them. Moreover, the RG tells us how the system behaves under coarse-graining when we are not at a non-trivial fixed point of the dynamics, e.g. below the critical point. In this case, coarse-graining would drive the system towards the trivial fixed point at  $\beta_T = 0$ . Deviations from scaling and theoretical estimate of exponents are typically associated with finite size effects, which can be taken into account via finite size scaling techniques. Therefore, exponents do not depend on the distance to criticality simply because they are not defined away from it.

In the brain, instead, we face a rather different scenario. First, we are out of equilibrium. Second, we do not know whether there is a genuine critical point or region

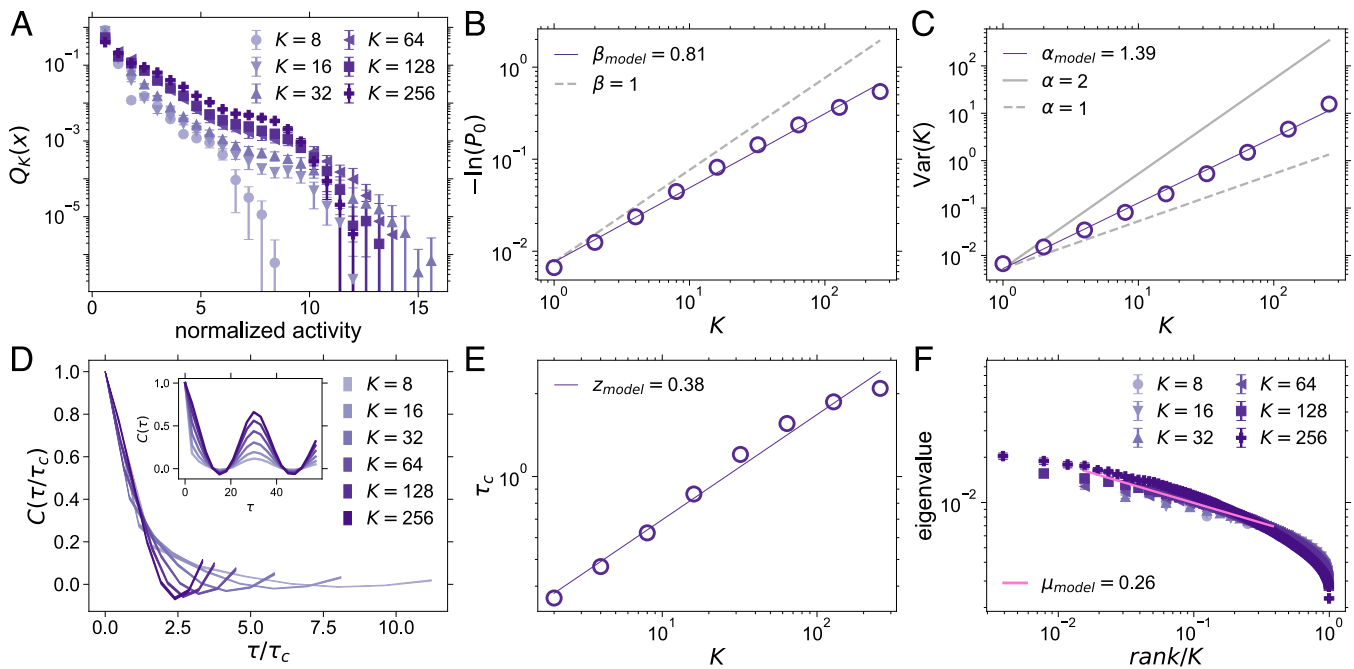


FIG. 5. **Non-Gaussian activity and scaling behaviors in the adaptive Ising model near criticality** **A.** Probability distributions of normalized non-zero activity for cluster sizes  $K \geq 8$ . Darker shades of red correspond to increasing cluster sizes. **B.** The log-probability of silence in coarse-grained variables ( $-\ln P_0$ ) as a function of cluster size ( $K$ ). The solid red line represents a linear least-squares fit of  $\log(-\ln P_0) = \beta_{model} \cdot \log K + b$  ( $\beta_{model} = 0.806 \pm 0.006$ , mean  $\pm$  SD). gray dashed line: prediction for independent variables. **C.** Variance (Var) of the non-normalized coarse-grained variables as a function of cluster size ( $K$ ). The solid red line corresponds to the linear least-squares fit,  $\log \text{Var}(K) = \alpha \cdot \log K + b$  ( $\alpha_{model} = 1.385 \pm 0.010$ ). gray dashed lines indicate reference growth rates: linear scaling for independent variables ( $\alpha = 1$ , bottom line) and quadratic scaling for fully correlated variables ( $\alpha = 2$ , top line). **D.** Average autocorrelation functions for different cluster sizes ( $K$ ) collapse onto a single curve after rescaling time by the corresponding auto-correlation time,  $\tau_c$ . Inset: Original autocorrelation functions before rescaling time. **E.** The autocorrelation time,  $\tau_c$ , increases with the cluster size as  $\tau_c \propto K^z$ . The solid red line shows the linear least-squares fit,  $\log \tau_c(K) = z \cdot \log K + b$  ( $z_{model} = 0.382 \pm 0.002$ ). **F.** Eigenvalues of covariance matrices for different cluster sizes,  $K$ . Larger clusters correspond to darker colors. The solid line is a least squares fit to  $\log \lambda = -\mu \cdot \log(\text{rank}/K) + b$  performed for  $K = 128$  on the range  $[2/128, 50/128]$  ( $\mu = 0.265 \pm 0.005$ , mean  $\pm$  SD). Simulations were performed on a fully connected network of 273000 neurons with  $\beta_T = 0.99$  and  $c = 0.01$ . Activity was “recorded” from  $N_s = 273$  subsystems each including 1000 spins. Results are averaged over  $n = 10$  simulations. Error bars (and shaded areas) represent SD and where not shown are smaller than the symbol size. The analysis is performed using  $e = \pm 3\text{SD}$  and  $\delta = 3dt$  (Appendix A).

[44] and, if so, what its nature is and what exponents we should expect to measure—including potential crossover phenomena that may occur out of equilibrium [45]. Empirical evidence, including those reported here, is consistent with critical dynamics. Biological considerations would then suggest a dynamical region within which the brain operates across physiological and functional states, and thus not necessarily presence of scaling behaviors only in a specific point and complete absence everywhere else. Last but importantly, we took a phenomenological approach to renormalization of neural data [31]. From the modeling perspective—an out-of-equilibrium one—, it seems then reasonable to ask whether and how the quantities we track across coarse-graining steps respond to proximity to criticality. Moreover, we notice that for quantities such as  $Q_K(x)$ ,  $P_0$ , and  $Var$ , the question is the nature of scaling rather than scaling itself. Once non-trivial scaling features are identified near criticality,

the role of biology (which may map in some way into RG symmetry and dimensionality arguments) in determining exponents becomes of interest, and we interrogated the model about that.

### III. DISCUSSION

We have shown that resting-state brain activity in humans is close to a non-trivial fixed point of a phenomenological renormalization group. Activity in coarse-grained clusters approaches a fixed non-Gaussian distribution as their sizes increase, while the probability of silence  $P_0$  (no activity) decreases sub-exponentially. The variance and autocorrelation of cluster activity both scale as a power-law of the cluster size, indicating a scale invariant structure of correlations in resting-state brain activity. This was further confirmed by the size-independent scal-

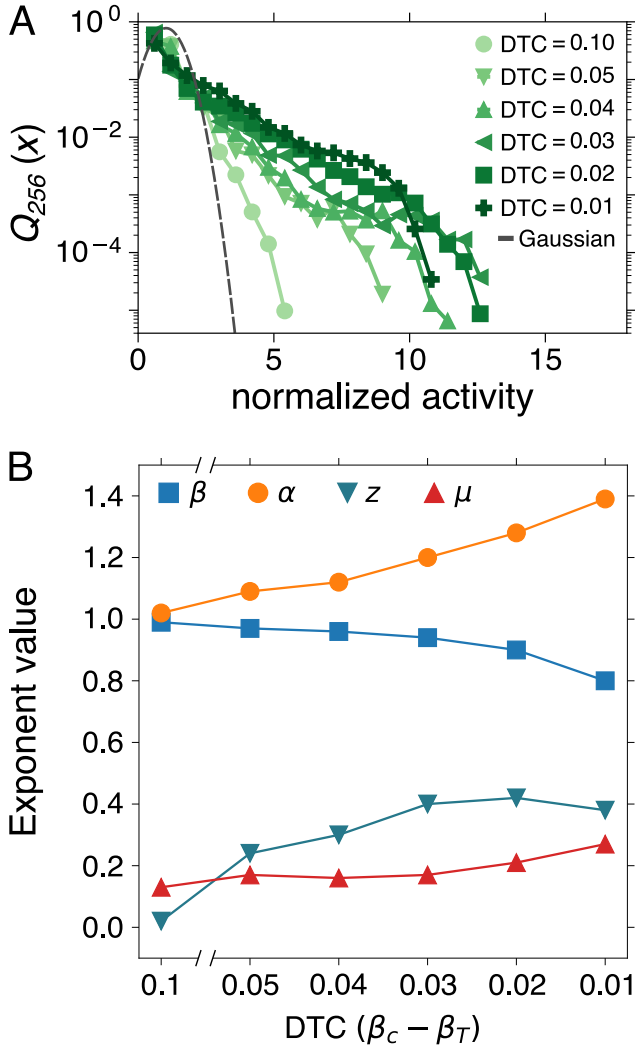


FIG. 6. **Distribution of activity and scaling exponents as a function of the distance to criticality in the adaptive Ising model.** **A.** Distribution of activity for cluster of size  $K = 256$ ,  $Q_{256}(x)$ , for increasing values of distance to criticality,  $DTC = \beta_c - \beta_T$ . The distribution is stable (non-Gaussian) in a narrow range of  $DTC \leq 0.03$ , and rapidly tend to a Gaussian for  $DTC > 0.04$ . A similar behavior is observed for smaller cluster size  $K$  (Fig. S20). **B.** The exponents controlling the scaling of silence and non-normalized activity variance,  $\beta$  and  $\alpha$ , rapidly approach 1 for increasing DTC. The exponent  $z$  and  $\mu$  both decrease for increasing DTC, and rapidly drop for  $DTC \geq 0.04$ .  $\mu$  drops to  $\approx 0.1$  already at  $DTC = 0.03$ .

ing of the eigenspectra of the cluster covariance matrices. In addition, we demonstrated that the scaling features of neuronal avalanches are invariant under the adopted coarse-graining scheme. The adaptive Ising model, with its two parameters inferred from data, suggests that empirical scaling exponents depend on the E/I balance of the network, paving the way for robust assessment of this key quantity in neuroscience research.

### A. Scaling in collective neural activity: from populations of neurons to fields

Evidence of a non-Gaussian fixed point in collective neural dynamics has recently been reported for population of neurons in the hippocampus [31], and over distinct regions of the mouse cortex [32, 33], with population activity showing consistent scaling features and signatures of non-Gaussianity. However, such reports were limited to the mouse brain and relatively small spatial scales.

In humans, access to neural population activity is still limited and most of neuroscience research is based on non-invasive electrophysiological recordings, such as electro- and magneto-encephalography. Both measures can be seen as an effective coarse-graining of neural activity, i.e. fields to which large populations of neurons contribute [35, 36]. Our analysis shows that these fields, although originating from filtered and highly non-linear superposition of neural/synaptic activity [36, 46], are collectively described by scaling laws that are remarkably similar—and in some cases comparable—to those observed in small populations of neurons. Despite the fact that we could not directly compare these findings with activity of spiking neurons in the human brain, our analysis indicates that collective behaviors of small- and large-scale neural activity are consistent and point to a non-trivial fixed point with common features. Recent analysis of BOLD fMRI in humans [34, 37] reported scaling exponents close to ours for the probability of silence ( $\beta$ ) and for the activity variance ( $\alpha$ ), and a relation between them similar to the one we measured in the MEG [37]. We also found robust scaling in the eigenspectra of the covariance matrices, with an exponent  $\mu$  that correlates with the scaling exponents  $\beta$  and  $\alpha$ . However, a close comparison with fMRI is difficult due, for instance, to the specific choice in the discretization threshold [34, 37].

That the MEG signals may carry over the same scaling properties of (local) populations of spiking neurons and, to some extent, even the same scaling exponents measured in a different species, is rather remarkable. However, our analysis indicates that simultaneous recording of spiking activity and fields, e.g. local field potentials, is needed to verify whether exponents are preserved across scales (and recorded signals) and species. In our approach, we consider only the extremes of all signal fluctuations above a certain threshold, and find that scaling behaviors are robust and persist from very low to very high values of the threshold, with an almost-complete decimation of the signals. While this could indicate that extreme events carry most information about underlying neural activity, we still observed scaling in all quantities when including in the analysis all the points belonging to the above-threshold excursions. However, all exponents changed significantly. In particular, the exponents  $\beta$  and  $z$  decreased, while  $\alpha$  and  $\mu$  increased (SM, Table II-III). Then, in the limit of continuous signals (Fig. S11), i.e.  $e \rightarrow 0$ , we found that, for increasing  $K$ , the cluster activity converges to the Gaussian core of the original signal

amplitude distribution, and all other analyzed quantities show no scaling, except for the activity variance that grows as  $\approx K^2$  over a range of  $K$  values (Fig. S11).

Overall, this indeed suggests that the relevant information about underlying neural dynamics is carried by high amplitude fluctuations. In contrast, small amplitude fluctuations within the Gaussian core of the signal amplitude distribution are mostly ‘noise’. To a large extent, coarse-graining seems to effectively ‘integrate out’ this noise, scaling behaviors being very robust even when a consistent part of that noise is included in the analysis (see Figs. S10, S14). However, scaling breaks down when all small fluctuations are included in the analysis (Fig. S11).

### B. Coarse-graining and avalanche criticality

The fields captured by MEG sensors across the scalp may have a significant overlap, and thus MEG signals tend to be highly correlated—even over relatively long distances [9]. Locally in particular, fields captured by nearest-neighbour sensors have a strong overlap. For this reason, in a correlation-based coarse-graining of the activity most of the sensors that are coupled, if not all, are likely those that are spatially close. Thus, one can expect that  $K$  clusters nucleate and grow in a localized area of the scalp until they are merged with other clusters that nucleated over a different area to form the few large clusters of the last steps of the PRG. If this intuition is correct, at least to some extent, then a coarse-graining strategy based on spatial proximity may provide similar results.

In [9], Shriki et al. proposed a coarse-graining of MEG sensor activity based on spatial proximity to study the stability of neuronal avalanche dynamics. They showed that, under such coarse-graining, the scaling behavior of avalanches was preserved. This is in line with our results on avalanche dynamics across coarse-graining steps (Fig. 4), and suggests that, for MEG data, the two procedures may be equivalent (at least to some extent).

The relation between scaling in coarse-grained brain activity and typical measures of brain criticality (or near-criticality) based on avalanche dynamics remain to be studied, and is not clear whether they provide a complementary picture of brain criticality. Our analysis shows that the difference  $|\frac{\alpha_t-1}{\tau_s-1} - \gamma|$  tends to zero for increasing cluster sizes (Fig. S17), indicating that the scaling relation  $\frac{\alpha_t-1}{\tau_s-1} = \gamma$  is satisfied. This suggests in turn that the system moves towards criticality [10]. Further, numerical simulations of the adaptive Ising model, although limited to a simplified scenario, suggest that avalanche criticality and scaling behaviors in resting-state activity coexist in a narrow subcritical region [39], as also suggested in [47]. However, analysis of dynamic quantities such as neuronal avalanches may require rescaling of time to properly assess scaling features (and their invariance) near criticality, as in dynamical RG [45].

### C. E/I balance and scaling behavior in the resting-state

The balance between excitation and inhibition is widely considered key for brain function, and has been linked to brain tuning to criticality [27, 48]. Yet, how to reliably assess the E/I ratio from non-invasive, large scale electrophysiological recordings remains an open challenge. Computational models indicate that the E/I ratio is connected with the exponent of the power-law decay of the spectral power [43, 49]. Our numerical results suggest that the E/I ratio is also linked to the scaling behaviors of resting-state activity under coarse-graining. The inferred adaptive Ising model, in which a negative feedback mimics the effect of inhibitory neural inputs [39], closely reproduced the scaling in silence probability, activity variance and correlation time, with the exponents  $\beta$ ,  $\alpha$  and  $z$  in quantitative agreement with the values measured in the resting MEG. As in the data, we found that the eigenspectrum of the covariance matrix decays as a power-law of the fractional ranks with a unique exponent  $\mu \approx 0.3$ , although smaller than the empirical value.

In the absence of negative feedback, the network is solely driven by excitatory interactions, and we observed that the exponents  $\beta$  and  $\alpha$  deviated significantly from the empirical values and both approached 1. At the same time, scaling of the activity autocorrelation time was disrupted, and eigenspectra were nearly flat and showed a poor data collapse for different  $K$ —in spite of proximity to criticality. These results suggest that alterations of the E/I balance could be assessed by measuring one of the scaling exponents  $\beta$ ,  $\alpha$  and  $\mu$ , the three of them being related (Fig. 3). This would be generally easier and more robust than estimating the scaling exponent of (often noisy) power spectra, where the scaling regime may not be unambiguously identifiable and crossover between different power-law regimes may exist [50].

Recently, scaling behaviors in neural activity have been suggested to emerge due to a slowly varying external drive [51, 52], as could be interpreted the time-varying global feedback and/or the all-to-all connectivity. However, we note that (i) the negative feedback is endogenous rather than external; (ii) non-homogeneous feedback are possible and do not disrupt scaling behaviors; (iii) we find similar scaling behaviors in 2D networks with nearest-neighbors interactions (Fig. S26). Furthermore, in the non-interacting, feedback-driven case, we find trivial scaling in activity variance and  $P_0$ , and no scaling in the other quantities (Fig. S25).

### D. Network dynamics and phenomenological renormalization

Although the model satisfactorily recapitulates most of the empirical PRG results, we openly acknowledge two quantitative shortfalls: (i) the distribution of cluster activity (non-Gaussian) deviates from the empirical distri-

bution, particularly on the tail, and collapse at large  $K$  is less robust than in empirical data (but improves significantly in the 2D scenario); (ii) the scaling exponent  $\mu$  of the eigenspectrum is significantly lower than the empirical value. Both these deviations from empirical data may depend on the over-simplified spatial structure of the model. We considered the simplest realization of the adaptive Ising class: uniform, all-to-all excitatory (ferromagnetic) connectivity and inhibitory drive (negative feedback). In this configuration, we are able to fit the two model parameters from data by matching analytical and empirical auto-correlations, and thus locate empirical data in the phase diagram of the model [39]. However, the underlying network is far from realistic. Furthermore, the comparison of collective behaviors between model and MEG data involves building subsystems of a certain size (number of neurons) to mimic the signals captured by MEG sensors, and fixing to additional parameters specific of the MEG data analysis, i.e., temporal bin and discretization threshold [18, 39]. These subsystems were disjoint and equally sized, creating an effective regular lattice with  $M$  units over which we performed coarse-graining of network activity. This setting may affect the correlation structure and, in turn, the eigenspectrum of the covariance matrix and the collective activity over large clusters  $K$  (leading, for instance, to deviations in the distribution of cluster activity). Despite these valid points of concern, this simple model shows a remarkable predictive power on the collective behaviors of the resting human brain, which also include avalanches and oscillations near criticality [39].

Future work should investigate the role of network connectivity (if any) in scaling behaviors and exponents, including more realistic topologies and inhibitory synapses. Our 2D simulations with nearest-neighbors interactions show scaling behaviors similar to those observed in the fully-connected network (mean-field), but quantitative agreement of  $\beta$  and  $z$  with empirical data is reduced (Fig. S26). Recent analysis in different areas of the mouse cortex showed quasi-universal scaling exponents, suggesting a weak dependence on network topologies [32]. However, it seems plausible, as also our and other models suggest [53], that these exponents depend on the qualitative nature of the connectivity and thus on network excitation-inhibition tuning, as observed for the scaling exponents of activity correlations, power spectra, and neuronal avalanches [16, 43, 48, 54, 55]. From a more theoretical perspective, the model could serve to investigate the connection between a phenomenological approach to renormalization and the renormalization group in this class of models.

## ACKNOWLEDGMENTS

FL acknowledges support from the European Union’s Horizon research and innovation program under the Marie Skłodowska-Curie Grant Agreement No.

101066790. FL and IT acknowledge support from the program TAlent in ReSeArch@University of Padua – STARS@UNIPD (project BRAINCIP—Brain criticality and information processing).

## DATA AND CODE AVAILABILITY

Data analyzed in this study were collected at the MEG facility of the NIH for a previously published study [9]. Data belongs to NIH and are available from O.S. (shrikio@bgu.ac.il) on reasonable request. Codes used in the current study are publicly available on GitHub. Data analysis: <https://github.com/lffrnt/CoarseGraining>. Model: [https://github.com/demartid/stat\\_mod\\_ada\\_nn](https://github.com/demartid/stat_mod_ada_nn).

## Appendix A: Data acquisition and pre-processing

Resting-state brain activity was recorded from 100 healthy participants in the MEG core facility at the NIMH (Bethesda, MD, USA) for a duration of 4 min (eyes closed). All experiments were carried out in accordance with NIH guidelines for human subjects. The sampling rate was 600 Hz, and the data were band-pass filtered between 1 and 150 Hz. Power-line interferences were removed using a 60 Hz notch filter designed in Matlab (Mathworks). The sensor array consisted of 275 axial first-order gradiometers. Two dysfunctional sensors were removed, leaving 273 sensors in the analysis. Analysis was performed directly on the axial gradiometer waveforms. The data analyzed here were selected from a set of MEG recordings for a previously published study [9], where further details can be found.

For each sensor, positive and negative excursions beyond a threshold  $e = \pm 3SD$  were identified. In each excursion beyond the threshold, a single event was identified at the most extreme value (maximum for positive excursions and minimum for negative excursions). For each signal, this resulted in a time series of number of events per time bin, including zeros, indicating absence of events in the bin. Comparison of the signal distribution with the best Gaussian fit indicates that the two distributions start to deviate from one another around  $\pm 2.7SD$  [9]. Thus, thresholds smaller than  $\pm 2.7SD$  would lead to the detection of many events related to noise in addition to real events whereas much larger thresholds would miss many of the real events. To avoid noise-related events while preserving most of the relevant events, in this study the threshold  $e$  was set at  $\pm 3.0SD$ . The raster of identified events was binned at a temporal resolution  $\delta = 1.67$ , the sampling frequency, and used for the PRG analysis. Stability of results with respect to thresholds, bin sizes, and definition of events is analyzed in Figs. S2-S4.

## Appendix B: Phenomenological Renormalization Group

### 1. Coarse-graining of brain activity

To work in the same data format that is used for the analysis of neuronal avalanches in MEG data, we performed coarse-graining on the binarized MEG signals, i.e. on the extreme events that are used to identify avalanches [9, 18]. At each step  $k$  of the PRG, which includes  $N_k$  variables  $x_i$  ( $i = 1, 2, \dots, N_k$ ), the entries of correlation coefficient matrix  $c_{ij}$  are calculated as

$$c_{ij} = \frac{\langle \delta x_i \delta x_j \rangle}{[\langle \delta x_i^2 \rangle \langle \delta x_j^2 \rangle]^{1/2}}, \quad (\text{B1})$$

where  $\delta x_i = x - \langle x_i \rangle$ . Then the most correlated pair  $(i, j)$  is identified by finding the largest non-diagonal element in the matrix, and the variables  $x_i$  and  $x_j$  are summed to define the new coarse-grained variable

$$x_i^{(K)} = Z_i^{(K)}(x_i^{(K/2)} + x_j^{(K/2)}), \quad (\text{B2})$$

where  $Z_i^{(K)} = 1/\langle x_i^{(K)} \rangle_{x_i \neq 0}$  is a normalization constant and  $K = 2^k$  indicates the cluster size at the step  $k$ , that is the number of original sensor signals that contribute to the variables  $x_i^{(K)}$  at the step  $k$  of the procedure. The notation  $\langle \rangle_{x_i \neq 0}$  indicates average over non-zero values. Normalization is such that the average number of extreme events in non-empty time bins is equal to one across all steps of the coarse-graining procedure. Each variable can only participate in one pair.

Thus, the pair  $(i, j)$  is removed and the next most correlated pair is identified until the original  $N_k$  variables have been grouped into  $N_k/2$  pairs. This procedure is iterated until  $N_k = 1$ , namely only a single variable is left. At each step  $k$  of the procedure, coarse-grained variables are the result of an iterative clustering of  $K = 2^k$  original sensors signals.

### 2. Distribution of activity and probability of silence in coarse-grained variables

The distribution of individual coarse-grained variables,  $P_K(x)$ , can be split into two contributions. The first one,  $Q_K(x)$ , is the probability of finding  $x \neq 0$  extreme events in non-empty time bins, i.e. time bin in which one detects at least one extreme event in the time series of coarse-grained variables resulting from clustering  $K$  MEG signals at the step  $k$  of the coarse-graining procedure. The second,  $P_0(K)$ , is the probability of finding a time bin with no extreme events (silence). The behavior of these two contributions is analyzed as a function of  $K$  (Fig. 2).

### 3. Mean activity and activity variance

The mean activity of coarse-grained variables,  $x_i^{(K)}$ , is

$$\langle x^{(K)} \rangle = \frac{1}{N_k} \sum_{i=1}^{N_k} \langle x_i^{(K)} \rangle = K \langle x^{(1)} \rangle, \quad (\text{B3})$$

and grows linearly with the mean of the original signals,  $\langle x^{(1)} \rangle$ . The variance of the non-normalized activity for cluster of size  $K$  is defined as

$$\text{Var}(K) = \frac{1}{N_k} \sum_{i=1}^{N_k} [\langle (x_i^{(K)})^2 \rangle - \langle x_i^{(K)} \rangle^2]. \quad (\text{B4})$$

For independent variables the variance grows linearly with the cluster size  $K$ , i.e.  $\text{Var}(K) \propto K$ . In the opposite case of fully correlated variables, the variance would grow quadratically with  $K$ , i.e.  $\text{Var}(K) \propto K^2$ , because of the maximally positive covariance between all variables. Scaling of the variance with  $K$  as  $\text{Var}(K) \propto K^\alpha$  with an intermediate value of the exponent alpha is indicative of a self-similar structure in the correlations, expected at criticality, and thus of a non-trivial fixed point in the renormalization group. Variance is calculated on non-normalized variables.

### 4. Autocorrelation $C(\tau)$ and correlation time $\tau_c$

The autocorrelation of activity in clusters of size  $K$  is defined as

$$C_i^{(K)}(\tau) = \frac{\langle \delta x_i^{(K)}(t_0) \delta x_i^{(K)}(t_0 + \tau) \rangle}{\text{Var}(x_i^{(K)})}. \quad (\text{B5})$$

The correlation time,  $\tau_c$ , is defined as the characteristic time of the exponential fit,  $y(t) = A \cdot e^{-t/\tau_c}$ , to  $C_K(\tau)$ , the average autocorrelation for the variables  $\{x_i^{(K)}\}$ . Under the hypothesis of dynamic scaling occurring near criticality, correlations scale with the cluster size  $K$ , and grow as a power-law of  $K$ ,  $\tau_c(K) \propto K^z$ , with  $z > 0$ . The exponential fit was performed in the range  $t \in [0, \tau_{max}]$ . For empirical data, we set  $\tau_{max} = 5$ , where  $C(\tau)$  approaches zero for most  $K$ . Increasing  $\tau_{max}$  does not significantly affect  $\tau_c$  and the scaling exponent  $z$ . A similar approach was used for numerical data in Fig. 5. In this case,  $\tau_{max} \in [5, 10]$  provided a good data collapse on the initial decay of  $C(\tau)$  over different  $K$ , and a stable scaling exponent  $z$ . For  $K$  and  $\tau_{max} > 10$ , due to increasing oscillatory trends, the initial exponential decay is followed by a slower decay of the autocorrelation, which can be described by an additional exponential term that modulates a sinusoidal function. In all cases,  $\tau_c$  refers to the time scale of the initial decay of the autocorrelation. In Figs. S22, S24, and S26, a double exponential fit was used, and  $\tau_c$  corresponds to the faster time scale.

## 5. Eigenspectrum of the covariance matrix

For each cluster size  $K$ , the eigenvalues of the corresponding covariance matrix are calculated as follows. First, the original sensors that contributed to each cluster of size  $K$  are retrieved. Then, the corresponding covariance matrix is calculated from the original binary activity (extreme events) of the sensors and the eigenspectrum obtained for each individual cluster. The representative eigenspectrum is the average over the  $N_k$  eigenspectra for the clusters of size  $K$ . The eigenvalues,  $\lambda$ , of the covariance matrix are ordered from the highest to the lowest. At a non-trivial fixed point of the renormalization group, as the one associated to criticality, one expects  $\lambda(\text{rank}) \propto 1/\text{rank}^\mu$  [31, 56]. The higher eigenvalues correspond to large wavelength (and low rank) and should ‘feel’ the system size, whereas smaller eigenvalues correspond to short wavelength (higher rank) and should not depend on the system size. As a consequence, for different cluster size  $K$ , one should have

$$\lambda \propto \left(\frac{\text{rank}}{K}\right)^{-\mu}. \quad (\text{B6})$$

The Eq.B6 implies: (i) the scaling of  $\lambda$  is independent of  $K$ ; (ii) when the rank is rescaled by  $K$  one observes a data collapse, i.e. all curves  $\lambda(\text{rank}/K)$  fall onto a single one (see Fig. 2F).

### Appendix C: Neuronal avalanches

For  $K = 1$  (no coarse-graining, original signals), an avalanche is defined as a continuous sequence of time bins,  $\delta$ , in which there is at least an event on any sensor, ending with at least a time bin with no events. The size of an avalanche,  $s$ , is given by the number of events in the avalanche; its duration,  $T$ , is given by the number of time bins belonging to the avalanche times  $\delta$ . For further details see [9, 18]. Avalanche analysis was performed on the original signals and in the first 4 PRG steps ( $K = 2, 4, 8, 16$ ), which retain a sufficient number of variables ( $N_2 = 136$ ,  $N_4 = 68$ ,  $N_8 = 34$ ,  $N_{16} = 17$ ) for avalanche statistics. For the coarse-grained variables ( $K \geq 2$ ), an event is defined as any non-zero activity in the time series. Then, avalanches follow the same definition as for non-coarse-grained signals ( $K = 1$ ).

### Appendix D: Surrogate data

#### 1. Surrogate MEG signals

*Phase randomization.* Random phase shuffling of the original continuous MEG signals is performed for each sensor independently. A Fourier transform of each sensor signal is performed, the corresponding phases are randomized while amplitudes are preserved. The surrogate signals are then obtained by performing an inverse

Fourier transform. The random phase shuffling destroys phase synchronization across cortical sites while preserving the linear properties of the original signals, such as power spectral density and two-point correlations [57].

*Trace randomization.* Trace shuffling is performed by applying a unique random permutation of the time points to all sensor signals. In this way, one destroys signal autocorrelations but preserves cross-correlations between MEG sensors. Together with phase randomization, this surrogate test allows one to disentangle the contribution of the sensor cross-correlation structure and local temporal dynamics to the observed collective behaviors.

#### 2. Random coarse graining.

Sensors are randomly paired without considering their actual cross-correlations. This test is performed for a single subject with 100 independent realizations of the random sensor pairing procedure. The full PRG analysis is repeated for each realization, and results are averaged across the 100 realizations. This test allows one to evaluate whether the observed results rely specifically on actual sensor-to-sensor correlations, rather than emerging from any hierarchical clustering of sensor activity.

### Appendix E: Further details on the Adaptive Ising model

The model is composed of a collection of  $N$  spins  $s_i = \pm 1$  ( $i = 1, 2, \dots, N$ ) that interact with each other with a coupling strength  $J_{ij}$ . In our analysis, the  $N$  spins represent excitatory neurons that are active when  $s_i = +1$  or inactive when  $s_i = -1$ , and  $J_{ij} > 0$ . Furthermore, we consider the fully homogeneous scenario, with neurons interacting with each other through synapses of equal strength  $J_{ij} = J = 1$ . The  $s_i$  are stochastically activated according to the Glauber dynamics, where the state of a neuron is drawn from the marginal Boltzmann-Gibbs distribution

$$P(s_i) \propto \exp(\beta \tilde{h}_i s_i) \quad \tilde{h}_i = \sum_j J_{ij} s_j + h_i \quad (\text{E1})$$

Spins experience an external field  $h$ , a negative feedback that depends on network activity according to the following equation,

$$\dot{h}_i = -c \frac{1}{|\mathcal{N}_i|} \sum_{j \in \mathcal{N}_i} s_j, \quad (\text{E2})$$

where  $c$  is a constant that controls the feedback strength, and the sum runs over a neighborhood of the neuron  $i$  specified by  $\mathcal{N}_i$ ; index  $j$  enumerates over all the elements of this neighborhood. Depending on the choice of  $\mathcal{N}_i$ , the feedback may depend on the activity of the neuron  $i$  itself (self-feedback), its nearest neighbors, or the entire

network—the case we considered in the main text. In a more realistic setting including both excitatory ( $J_{ij} > 0$ ) and inhibitory neurons ( $J_{ij} < 0$ ), one could then take into account the different structural and functional properties of excitatory and inhibitory neurons by considering different interaction and feedback properties [58]. In our simulations, one time step,  $dt$ , corresponds to one system sweep—i.e.  $N$  spin flips—of Monte Carlo updates, and Eq (E2) is integrated using  $\Delta t = 1/N$ . Note that this

choice of timescales for deterministic vs stochastic dynamic is important, as it interpolates between the quasi-equilibrium regime where spins fully equilibrate with respect to the field  $h$ , and the regime where the field is updated by feedback after each spin-flip and so spins can constantly remain out of equilibrium.  $\Delta t$  is generally much smaller than the characteristic time of the adaptive feedback that is controlled by the parameter  $c$ .

Model data analysis followed the same procedure illustrated for empirical data.

- 
- [1] L. de Arcangelis, F. Lombardi, and H. J. Herrmann, Criticality in the brain, *Journal of Statistical Mechanics: Theory and Experiment* **2014**, P03026 (2014).
- [2] V. Zimmern, Why brain criticality is clinically relevant: a scoping review, *Frontiers in neural circuits* **14**, 54 (2020).
- [3] K. B. Hengen and W. L. Shew, Is criticality a unified set-point of brain function?, *Neuron* **113**, 2582 (2025).
- [4] I. Algom and O. Shriki, The concrit framework: Critical brain dynamics as a unifying mechanistic framework for theories of consciousness, *Neuroscience & Biobehavioral Reviews* **180**, 106483 (2026).
- [5] B. G. Cragg and H. N. Temperley, The organization of neurones: a cooperative analogy, *EEG Clin. Neurophysiol.* **6**, 85 (1954).
- [6] H. E. Stanley, *Introduction to phase transition and critical phenomena* (Oxford Univ. Press, New York, 1971).
- [7] J. M. Beggs and D. Plenz, Neuronal avalanches in neocortical circuits, *J. Neurosci.* **23**, 11167 (2003).
- [8] T. Petermann, T. C. Thiagarajan, M. Lebedev, M. Nicolelis, D. R. Chialvo, and D. Plenz, Spontaneous cortical activity in awake monkeys composed of neuronal avalanches, *Proc Natl Acad Sci USA* **106**, 15921 (2009).
- [9] O. Shriki, J. Alstott, F. Carver, T. Holroyd, R. N. A. Hanson, M. L. Smith, R. Coppola, E. Bullmore, and D. Plenz, Neuronal avalanches in the resting meg of the human brain, *J. Neurosci.* **33**, 7079 (2013).
- [10] A. J. Fontenele, N. A. P. de Vasconcelos, T. Feliciano, L. A. A. Aguiar, C. Soares-Cunha, B. Coimbra, L. D. Porta, S. Ribeiro, A. J. Rodrigues, N. Sousa, P. V. Carelli, and M. Copelli, Criticality between cortical states, *Phys. Rev. Lett.* **122**, 208101 (2019).
- [11] S. Scarpetta, N. Morisi, C. Mutti, N. Azzi, I. Trippi, R. Ciliento, I. Apicella, G. Messuti, M. Angiolelli, F. Lombardi, *et al.*, Criticality of neuronal avalanches in human sleep and their relationship with sleep macro- and micro-architecture, *Iscience* **26** (2023).
- [12] D. R. W. Burrows, G. Diana, B. Pimpel, F. Moeller, M. P. Richardson, D. S. Bassett, M. P. Meyer, and R. E. Rosch, Microscale neuronal activity collectively drives chaotic and inflexible dynamics at the macroscale in seizures, *Journal of Neuroscience* **43**, 3259 (2023).
- [13] K. Linkenkaer-Hansen, V. V. Nikouline, J. M. Palva, and R. J. Ilmoniemi, Long-range temporal correlations and scaling behavior in human brain oscillations, *Journal of Neuroscience* **21**, 1370 (2001).
- [14] S. Thurner, C. Windischberger, E. Moser, P. Walla, and M. Barth, Scaling laws and persistence in human brain activity, *Physica A: Statistical Mechanics and its Applications* **326**, 511 (2003).
- [15] K. Linkenkaer-Hansen, S. Monto, H. Ryttsälä, K. Suominen, E. Isometsä, and S. Kähkönen, Breakdown of long-range temporal correlations in theta oscillations in patients with major depressive disorder, *J. Neurosci.* **25**, 10131 (2005).
- [16] J. M. Palva, A. Zhigalov, J. Hirvonen, O. Korhonen, K. Linkenkaer-Hansen, and S. Palva, Neuronal long-range temporal correlations and avalanche dynamics are correlated with behavioral scaling laws, *Proc. Natl. Acad. Sci. USA* **110**, 3585 (2013).
- [17] C. Meisel, K. Bailey, P. Achermann, and D. Plenz, Decline of long-range temporal correlations in the human brain during sustained wakefulness, *Scientific Reports* **7**, 11825 (2017).
- [18] F. Lombardi, O. Shriki, H. J. Herrmann, and L. de Arcangelis, Long-range temporal correlations in the broadband resting state activity of the human brain revealed by neuronal avalanches, *Neurocomputing* **461**, 657 (2021).
- [19] F. Lombardi, M. Gomez-Extremera, P. Bernaola-Galvan, R. Vetrivelan, C. B. Saper, T. E. Scammell, and P. C. Ivanov, Critical dynamics and coupling in bursts of cortical rhythms indicate non-homeostatic mechanism for sleep-stage transitions and dual role of vlpo neurons in both sleep and wake, *J. Neurosci.* **40**, 171 (2020).
- [20] J. W. J. L. Wang, F. Lombardi, X. Zhang, C. Anacleto, and P. C. Ivanov, Non-equilibrium critical dynamics of bursts in  $\theta$  and  $\delta$  rhythms as fundamental characteristic of sleep and wake micro-architecture, *PLoS computational biology* **15**, e1007268 (2019).
- [21] C. Huo, F. Lombardi, C. Blanco-Centurion, P. J. Shirromani, and P. C. Ivanov, Role of the locus coeruleus arousal promoting neurons in maintaining brain criticality across the sleep-wake cycle, *Journal of Neuroscience* **44** (2024).
- [22] A. Levina, J. M. Herrmann, and T. Geisel, Dynamical synapses causing self-organized criticality in neural networks, *Nature physics* **3**, 857 (2007).
- [23] G. Menesse, B. Marin, M. Girardi-Schappo, and O. Kinouchi, Homeostatic criticality in neural networks, *Chaos, Solitons & Fractals* **156**, 111877 (2022).
- [24] L. J. Fosque, A. Alipour, M. Zare, R. V. Williams-García, J. M. Beggs, and G. Ortiz, Quasicriticality explains variability of human neural dynamics across life span, *Frontiers in Computational Neuroscience* **16**, 1037550 (2022).
- [25] G. Tkačik, T. Mora, O. Marre, D. Amodè, S. E. Palmer, M. J. Berry, and W. Bialek, Thermodynamics and signatures of criticality in a network of neurons, *Proceedings of the National Academy of Sciences* **112**, 11508 (2015).
- [26] T. Mora, S. Deny, and O. Marre, Dynamical criticality in

- the collective activity of a population of retinal neurons, *Physical review letters* **114**, 078105 (2015).
- [27] T. S. A. N. Simões, F. Lombardi, D. Plenz, H. J. Herrmann, and L. de Arcangelis, Maximum entropy models of neuronal populations at and off criticality (2025), arXiv:2511.14872.
- [28] G. Tkačik, O. Marre, D. Amodei, E. Schneidman, W. Bialek, and M. J. Berry, Searching for collective behavior in a large network of sensory neurons, *PLoS computational biology* **10**, e1003408 (2014).
- [29] J. Cardy, *Scaling and Renormalization in Statistical Physics*, Cambridge Lecture Notes in Physics (Cambridge University Press, 1996).
- [30] L. Kadanoff, Scaling at critical points, in *Phase transitions and critical phenomena, vol. 5A*, edited by C. Domb and M. Green (Academic Press, London, 1976).
- [31] L. Meshulam, J. L. Gauthier, C. D. Brody, D. W. Tank, and W. Bialek, Coarse graining, fixed points, and scaling in a large population of neurons, *Phys. Rev. Lett.* **123**, 178103 (2019).
- [32] G. B. Morales, S. Di Santo, and M. A. Muñoz, Quasiuniversal scaling in mouse-brain neuronal activity stems from edge-of-instability critical dynamics, *Proceedings of the National Academy of Sciences* **120**, e2208998120 (2023).
- [33] G. G. Cambrainha, D. M. Castro, N. A. P. de Vasconcelos, P. V. Carelli, and M. Copelli, Criticality at work: Scaling in the mouse cortex enhances performance, *PRX Life* **3**, 033026 (2025).
- [34] A. Ponce-Alvarez, M. L. Kringelbach, and G. Deco, Critical scaling of whole-brain resting-state dynamics, *Communications Biology* **6**, 627 (2023).
- [35] G. Pfurtscheller and F. H. L. da Silva, Event-related eeg/meg synchronization and desynchronization: basic principles, *Clin. Neurophysiol.* **110**, 1842 (1999).
- [36] C. J. Stam, Nonlinear dynamical analysis of eeg and meg: review of an emerging field, *Clinical Neurophysiology* **116**, 2266 (2005).
- [37] D. M. Castro, E. P. Raposo, M. Copelli, and F. A. N. Santos, Interdependent scaling exponents in the human brain, *Phys. Rev. Lett.* **135**, 198401 (2025).
- [38] R. D. Cook, Detection of influential observation in linear regression, *Technometrics* **19**, 15 (1977).
- [39] F. Lombardi, S. Pepić, O. Shriki, G. Tkačik, and D. De Martino, Statistical modeling of adaptive neural networks explains co-existence of avalanches and oscillations in resting human brain, *Nature Computational Science* **3**, 254 (2023).
- [40] D. De Martino, Feedback-induced self-oscillations in large interacting systems subjected to phase transitions, *J. Phys. A* **52**, 045002 (2019).
- [41] F. Lombardi and D. De Martino, Oscillations and avalanches coexist in brain networks close to criticality, *Nat Comput Sci* **3**, 194 (2023).
- [42] S. Di Santo, P. Villegas, R. Burioni, and M. A. Munoz, Landau–ginzburg theory of cortex dynamics: Scale-free avalanches emerge at the edge of synchronization, *Proc Natl Acad Sci USA* **115**, E1356–E1365 (2018).
- [43] F. Lombardi, H. J. Herrmann, and L. de Arcangelis, Balance between excitation and inhibition determines 1/f power spectrum in neuronal networks, *Chaos* **27**, 047402 (2017).
- [44] P. Moretti and M. A. Munoz, Griffiths phases and the stretching of criticality in brain networks, *Nat. Commun.* **4**, 2521 (2013).
- [45] U. C. Täuber, *Critical Dynamics: A Field Theory Approach to Equilibrium and Non-Equilibrium Scaling Behavior* (Cambridge University Press, 2014).
- [46] N. Dehghani, C. Bedard, S. S. Cash, E. Halgren, and A. Destexhe, Comparative power spectral analysis of simultaneous electroencephalographic and magnetoencephalographic recordings in humans, *J. Comput. Neurosci.* **21**, 405 (2010).
- [47] R. Calvo, C. Martorell, A. Roig, and M. A. Muñoz, Robust scaling in human brain dynamics despite correlated inputs and limited sampling distortions, *Physical Review Letters* **136**, 10.1103/36v9-wtm8 (2026).
- [48] W. Shew, H. Yang, T. Petermann, R. Roy, and D. Plenz, Neuronal avalanches imply maximum dynamic range in cortical networks at criticality, *J. Neurosci.* **29**, 15595 (2009).
- [49] R. Gao, E. J. Peterson, and B. Voytek, Inferring synaptic excitation/inhibition balance from field potentials, *NeuroImage* **158**, 70 (2017).
- [50] B. J. He, Scale-free brain activity: past, present, and future, *Trends in Cognitive Sciences* **18**, 480 (2014).
- [51] M. C. Morrell, A. J. Sederberg, and I. Nemenman, Latent dynamical variables produce signatures of spatiotemporal criticality in large biological systems, *Phys. Rev. Lett.* **126**, 118302 (2021).
- [52] B. Mariani, G. Nicoletti, M. Bisio, M. Maschietto, S. Vasanelli, and S. Suweis, Disentangling the critical signatures of neural activity, *Sci. Rep.* **12** (2022).
- [53] Y. Hu and H. Sompolinsky, The spectrum of covariance matrices of randomly connected recurrent neuronal networks with linear dynamics, *PLoS Comput Biol* **18**, e1010327 (2022).
- [54] F. Lombardi, H. J. Herrmann, D. Plenz, and L. de Arcangelis, Temporal correlations in avalanche occurrence, *Sci. Rep.* **6**, 24690; doi: 10.1038/srep24690 (2016).
- [55] T. Fekete, D. Omer, K. O’Hashi, A. Grinvald, C. van Leewen, and O. Shriki, Critical dynamics, anesthesia and information integration: Lessons from multi-scale criticality analysis of voltage imaging data, *NeuroImage* **183**, 919 (2018).
- [56] S. Bradde and W. Bialek, Pca meets rg, *Journal of Statistical Physics* **167**, 462–475 (2017).
- [57] J. Theiler, S. Eubank, A. Longtin, B. Galdrikian, and J. D. Farmer, Testing nonlinearity in time series: the method of surrogate data, *Physica D* **58**, 77 (1992).
- [58] P. Bonifazi, M. Goldin, M. A. Picardo, I. Jorquera, A. Cattani, G. Bianconi, A. Represa, Y. Ben-Ari, and R. Cossart, Gabaergic hub neurons orchestrate synchrony in developing hippocampal networks, *Science* **326**, 1419 (2009).
- [59] J. Alstott, E. Bullmore, and D. Plenz, powerlaw: A python package for analysis of heavy-tailed distributions, *PLoS one* **9**, e85777 (2014).

## Supplementary Materials

## SUPPLEMENTARY FIGURES

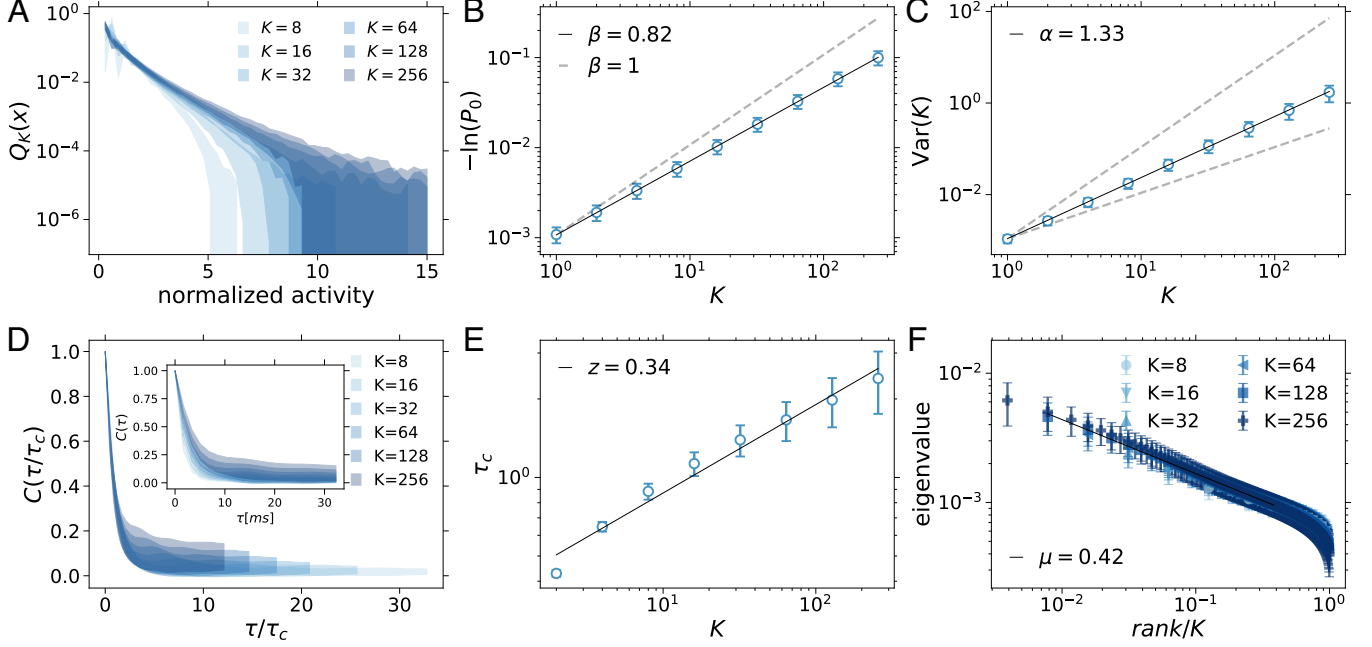


Fig. S1. **PRG analysis of resting state brain activity shows little variability across subjects.** **A.** Average probability distribution for normalized nonzero activity for the cluster sizes  $K \geq 8$ . Darker blue = Increasing cluster size. **B.** Average log-probability of silence in coarse-grained variables ( $\ln P_0$ ) as a function of cluster size,  $K$  ( $n = 100$ ). The solid black line represents a linear least-squares fit of  $\log(-\ln P_0) = \log \cdot K^\beta + b$ , where  $\beta = 0.82 \pm 0.002$  (fit  $\pm$  error on the fit) The gray dashed line indicates prediction for independent variables. **C.** Average variance (Var) of the non-normalized coarse-grained variables across  $n = 100$  subjects as a function of the cluster size,  $K$ . The solid black line corresponds to the linear least-square fit,  $\log \text{Var}(K) = \alpha \cdot \log K + b$ , where  $\alpha = 1.33 \pm 0.005$  (fit  $\pm$  error on the fit). gray dashed lines indicate reference growth rates: linear scaling ( $\alpha = 1$ ) characteristic of independent variables and quadratic scaling ( $\alpha = 2$ ) expected for fully correlated variables. **D.** Average correlation functions ( $n = 100$ ) for different cluster sizes,  $K$ , collapse on a single curve after rescaling time,  $\tau$ , by the correlation time  $\tau_c$ . Inset: Original autocorrelation for different  $K$ . **E.** The autocorrelation time,  $\tau_c$ , as a function of  $K$ , grows as  $\tau_c \propto K^z$ . The solid black line corresponds to the linear least-square fit,  $\log \tau_c(K) = z \cdot \log K + b$ , where  $z = 0.34 \pm 0.02$  (fit  $\pm$  error on the fit). **F.** Eigenvalues of cluster covariance matrices for different cluster sizes. Results are averaged over  $n = 100$  subjects. Larger clusters correspond to darker colors. The solid line is a least squares fit to  $\log \lambda = \log b(\text{rank}/K)^{-\mu}$  performed for  $K = 128$ . The fitting range is  $2/128 - 50/128$ . All results are averaged over  $n = 100$  subjects. Error bars and shaded areas represent standard deviation (SD).

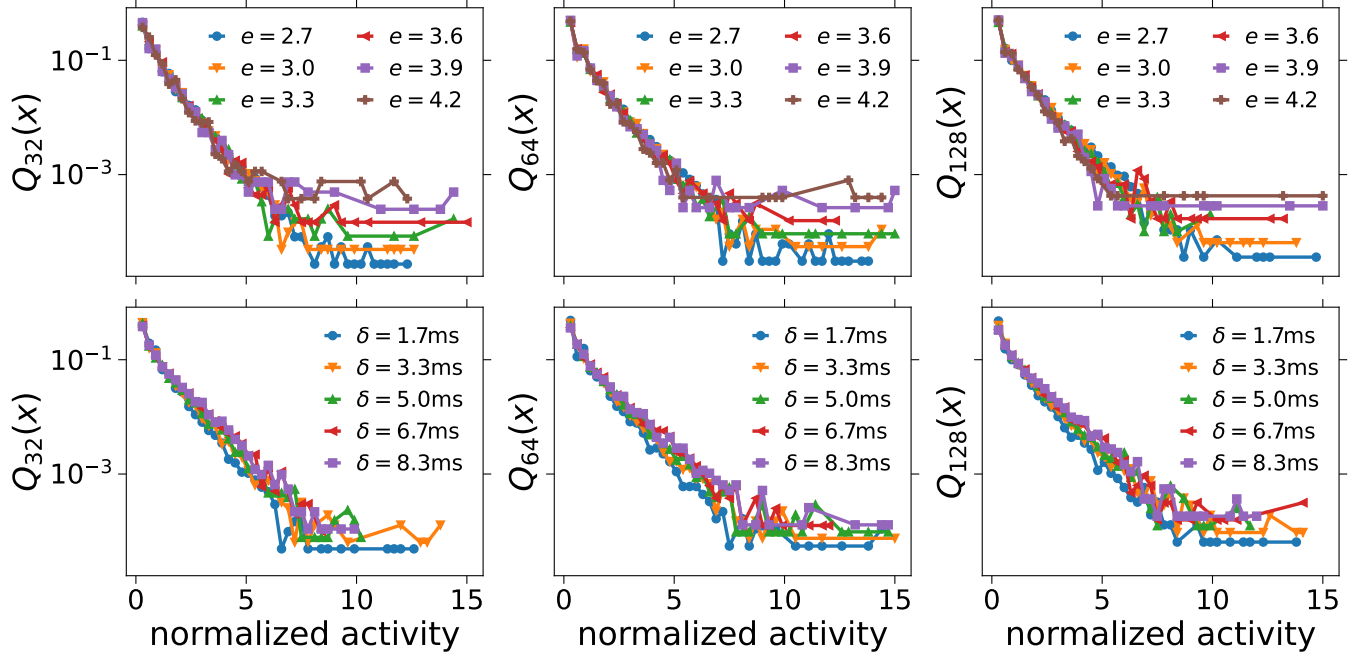


Fig. S2. **Distribution of normalized cluster activity is independent of the binarization threshold,  $e$ , and bin size  $\delta$ .** **Top row.** Distribution of normalized cluster activity for  $K = 32$ ,  $K = 64$ , and  $K = 128$  for different values of the binarization threshold  $e$ . **Bottom row.** Distribution of normalized cluster activity for  $K = 32$ ,  $K = 64$ , and  $K = 128$  for different bin sizes  $\delta$ .

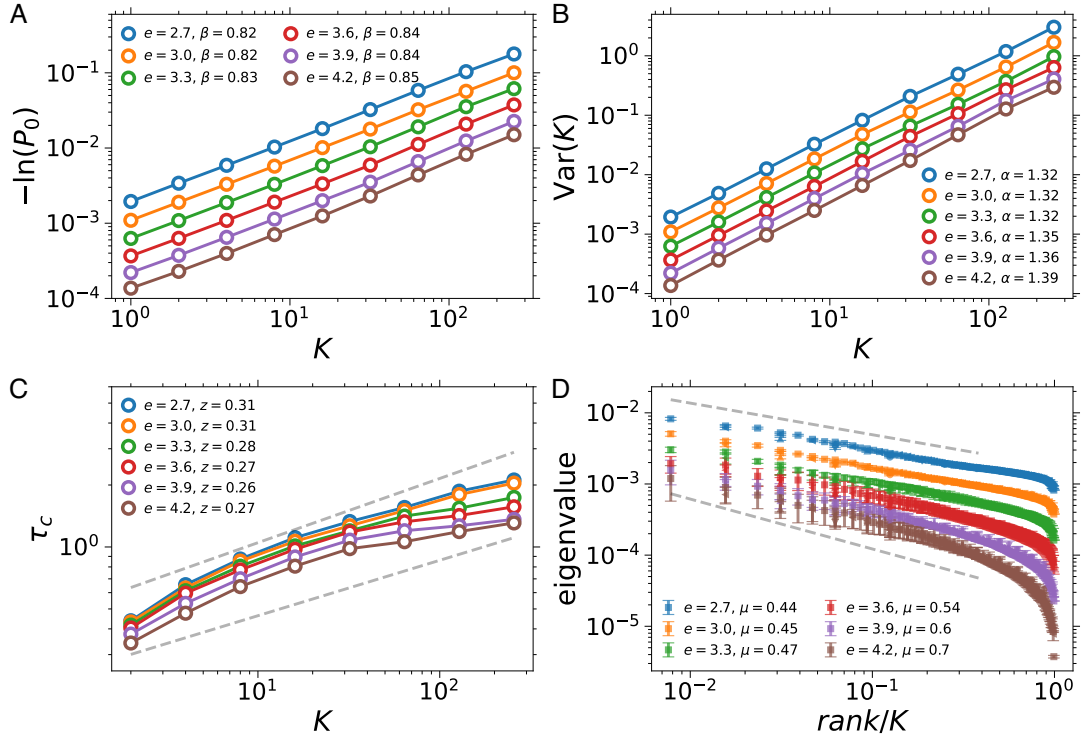


Fig. S3. **Robustness of scaling behaviors with respect to data binarization threshold.** **A.** Distributions of silence robustly follow the the functional form  $P_0(K) = e^{-aK^\beta}$  for a range of binarization threshold  $2.7 \leq e \leq 4.2$  SD. The exponent  $\beta$  is stable, and shows small variability,  $0.82 \leq \beta \leq 0.85$ , increasing for higher thresholds. This is expected since more and more points are removed from the timeseries as one increases the threshold. **B.** Scaling of the variance  $\text{Var}(K)$  with  $K$  is robust and shows little dependence on binarization threshold  $e$ . **C.** Autocorrelation time,  $\tau_c$ , as a function of  $K$ . Deviations from scaling are observed for higher thresholds  $e$  at large cluster sizes,  $K > 64$ . This must be ascribed to increasing sparsity of time series (or increasing sub-sampling), which weakens original correlations. **D.** Dependence of eigenvalue spectra on the threshold  $e$ . Scaling and exponent are robust for a range of  $e$  values. Deviations are observed for  $e \geq 3.9$ . We notice that, for a given cluster size, variability across clusters increases for increasing thresholds  $e$ . All quantities are calculated for an individual subject with bin size  $\delta = 1.67$  ms, the sampling time. Results are consistent across subjects.

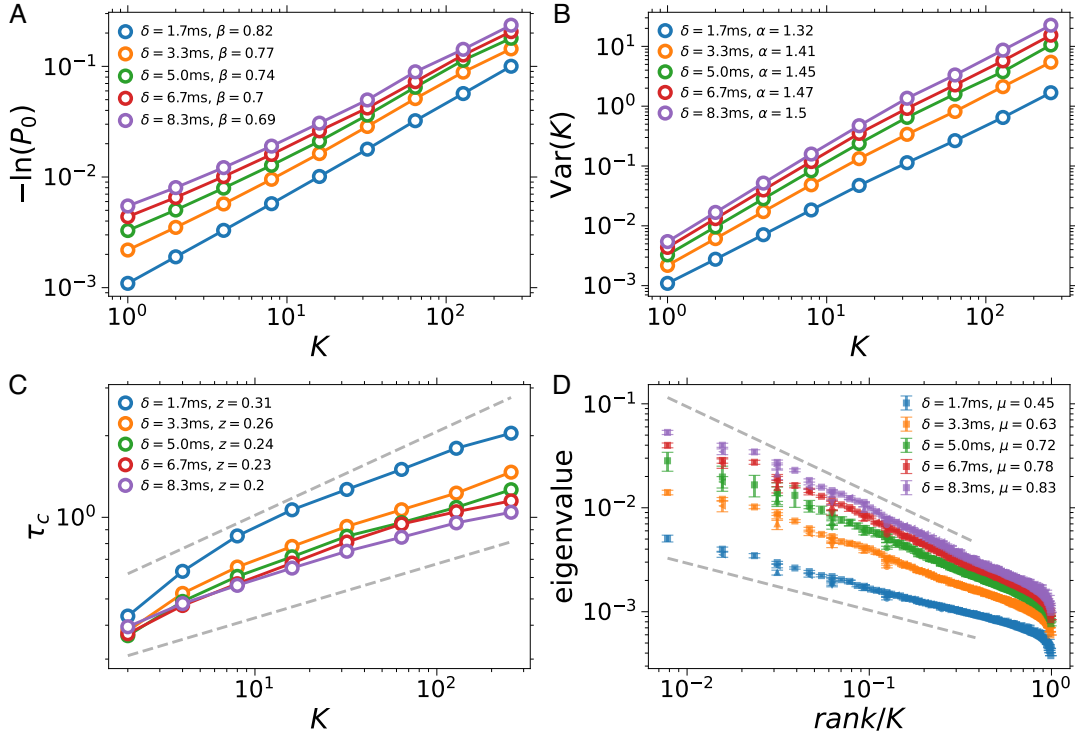


Fig. S4. **Dependence of scaling behaviors on data binning.** **A.** Distributions of silence follow the functional form  $P_0(K) = e^{-aK^\beta}$  in the range of time bin sizes from  $1T_s$  to  $5T_s$ , where  $T_s = 1/600\text{s}$  is the sampling time. The exponent  $\beta$  tends to decrease for increasing bin sizes, and goes from 0.82 at  $\delta = 1T_s$  to  $\beta = 0.69$  at  $\delta = 5T_s$ . Time binning mostly affects behavior at  $K \leq 8$ . **B.** The scaling exponent of the variance,  $\alpha$ , increases with the bin size  $\delta$ . Although rather limited, this increase indicates that binning increases correlations among variables. **C.** Autocorrelation time,  $\tau_c$ , as a function of  $K$ . For  $\delta = 1T_s$ ,  $\tau_c$  is consistently larger than for larger bin sizes. Asymptotic scaling (large  $K$ ) is well preserved across bin sizes. Small changes in the scaling exponent  $z$  are mostly due to effects of binning on autocorrelation at small  $K$ . As for  $P_0$ , time binning mostly affects  $\tau_c$  scaling at small cluster sizes  $K$ . **D.** The scaling and exponent of the eigenvalue spectrum depends on time binning. The exponent  $\mu$  increases with  $\delta$ . Difference in  $\mu$  is particularly marked between  $\delta = 1T_s$  (no time binning) and  $\delta = 2T_s = 3.3$  ms. Dashed lines represent the fit for  $\delta = 1T_s = 1.7$  ms and  $\delta = 5T_s = 8.3$  ms. All quantities are calculated for an individual subject and threshold 3 SD. Results are consistent across subjects.

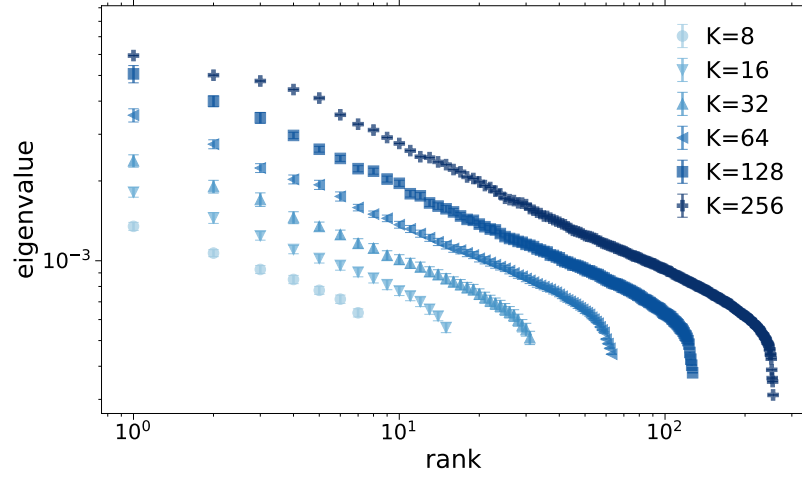


Fig. S5. **Eigenspectra of the covariance matrix for different cluster size  $K$ .** Eigenvalues  $\lambda$  as a function of their ranks (not rescaled by the cluster size  $K$ ).

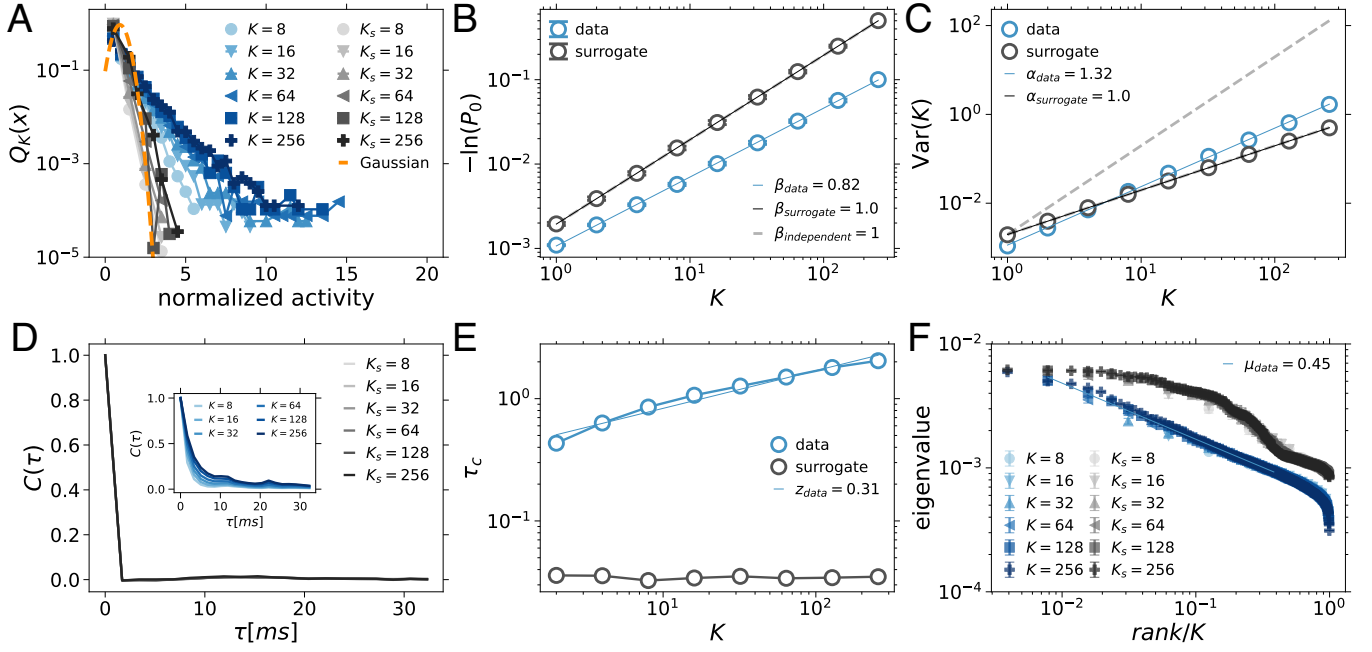


Fig. S6. **Renormalization group analysis of phase randomized MEG signals (individual subject).** **A.** Probability distribution for normalized non-zero activity for the cluster sizes  $K \geq 8$ . Darker color = Increasing cluster size. Gray scale: phase-randomized data. In blue: original data. **B.** Probability of silence in coarse-grained variables ( $-\ln P_0$ ) as a function of the cluster size,  $K$ . Probability of silence decays as  $P_0(K) = e^{-bK^\beta}$  with  $\beta = 1$  in case of phase randomized signals (solid black line), as for independent variables. For the original data,  $\beta_{data} = 0.82$  (blue solid line). Error bars represent SEM and are calculated across coarse-grained variables for the corresponding  $K$ . **C.** Variance ( $\text{Var}$ ) of the coarse-grained variables as a function of the cluster size,  $K$ . The solid lines correspond to linear least-square fits,  $\log \text{Var}(K) = \alpha \cdot \log K + b$ . For phase randomized data  $\alpha = 1$  (solid black line), while for original data  $\alpha = 1.32$ . gray dashed lines correspond to  $\text{Var}(K) \sim K^2$ . **D.** Average correlation functions for different cluster sizes,  $K$ , of the phase randomized data. Autocorrelation is independent of  $K$  and shows a very fast decay to zero. Inset: Autocorrelation for the original data. **E.** The autocorrelation time,  $\tau_c$ , is independent of  $K$  for the phase randomized data (black circles). For the original data  $\tau_c \propto K^z$ . The solid blue line corresponds to the linear least-square fit,  $\log \tau_c(K) = z \cdot \log K + b$ , where  $z = 0.31$ . **F.** Eigenvalues of covariance matrices within clusters for different cluster sizes. For randomized data (gray scale), scaling is disrupted. Larger clusters correspond to darker colors. Original data are shown in blue. Solid blue line: least squares fit to  $\log \lambda = \log b(\text{rank}/K)^{-\mu}$  performed for  $K = 128$ . The fitting range is  $2/128 - 50/128$ . Error bars represent SEM.

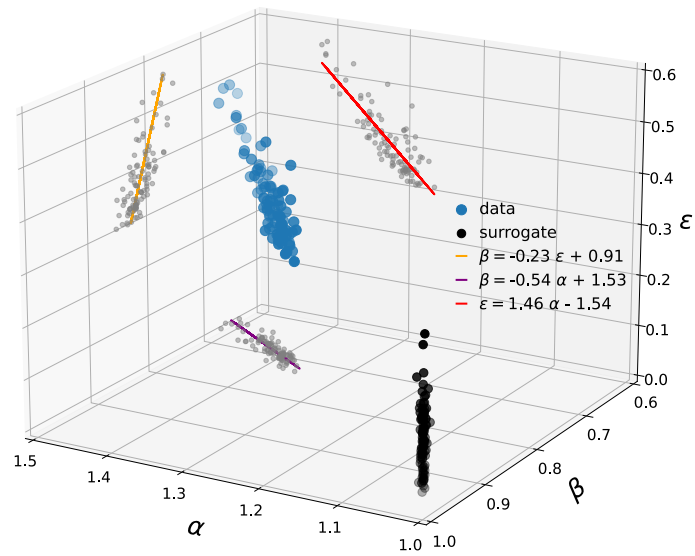


Fig. S7. Relationships between scaling exponents,  $\alpha$ ,  $\beta$ , and  $\epsilon$  in original and surrogate MEG data. Exponent relationships for original and phase-randomized data (black dots).

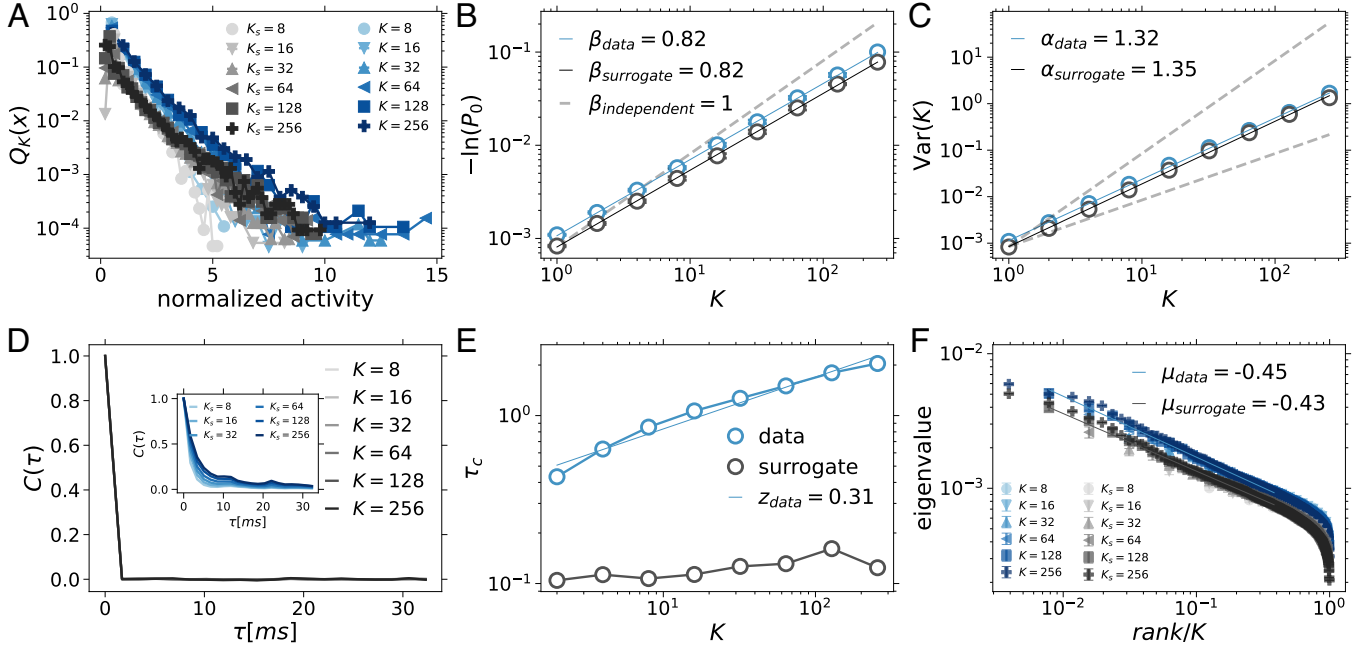


Fig. S8. **Renormalization group analysis of trace randomized MEG signals.** Trace randomized data are obtained by random shuffling of signal amplitudes for all MEG sensors (Appendix D). All signal timeseries are shuffled using the same random permutation of time indices. Unlike in the phase randomized data, the distributions of normalized activity approaches a non-Gaussian form for increasing  $K$  (A, black-gray scale). The probability of silence scales with  $K$  as for the original data, i.e.  $P_0(K) = e^{-bK^\beta}$  with  $\beta = 0.82$  (B). Similarly, the variance of coarse-grained variables as a function of  $K$  scales as  $Var(K) \sim K^\alpha$ , with  $\alpha = 1.32$  as for the original data (C). On the other hand, the autocorrelation time,  $\tau_c$ , is very short (D, main panel) and is independent of  $K$  as for trace randomized data (E). For the original data  $\tau_c \propto K^z$ , with  $z = 0.31$ , while  $z \approx 0$  for phase randomized data. For trace randomized data (gray scale), the exponent  $\mu = 0.45$  of the eigenvalue spectra is as in the original data (F). In all panels, original data are shown in blue and randomized data in black. Larger clusters correspond to darker shades of colors. Solid lines in B, C, and E are linear least-square fit of the form  $\log y = a \cdot \log x + b$ , where  $x = K$  and  $y = -\ln P_0$ ,  $Var(K)$  and  $\tau_c$ , respectively. Solid blue and black line in F: least squares fit to  $\log \lambda = \log b(\text{rank}/K)^{-\mu}$  performed for  $K = 128$ . The fitting range is  $2/128 - 50/128$ . Error bars represent SEM.

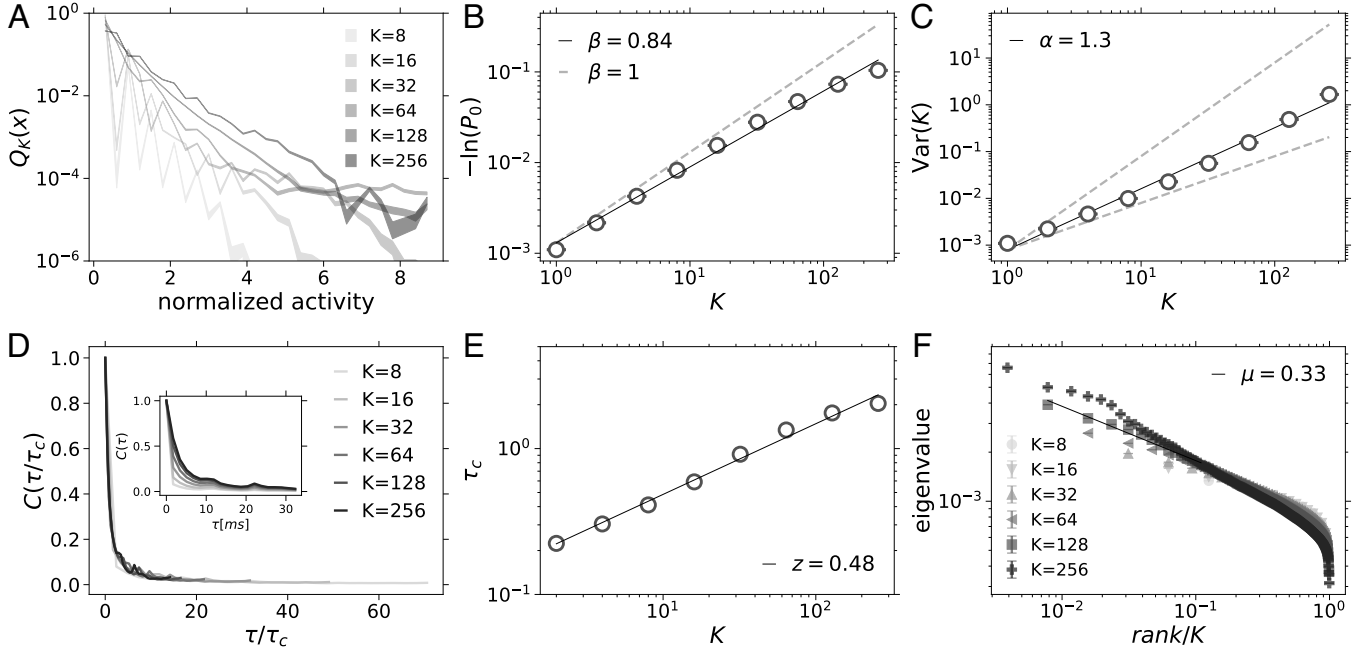


Fig. S9. **Renormalization group analysis with random pairing of MEG sensors.** In random pairing variables are not combined according to their correlations. Each variable is uniquely paired with another variable that is selected randomly (Methods). **A.** Distributions of normalized activity for  $K \geq 8$ . **B.** Probability of silence,  $P_0$ , as a function of  $K$ . **C.** Variance of non-normalized coarse-grained variables as a function of  $K$ . **D.** Average autocorrelation for clusters of size  $K \geq 8$ . **E.** Autocorrelation time  $\tau_c$  as a function of  $K$ . **F.** Eigenvalue spectra for  $K \geq 8$ . Despite random pairing many of the scaling features observed in original data seem to be preserved (see B, C, E), with slight changes in the exponents. Scaling is also observed in the eigenvalue spectra, although the exponent appear to depend on  $K$ . The exponent for  $K = 128$  is  $\mu = 0.37$  (fitting range: 2-50). The distribution  $Q_K(x)$  tends to a non-Gaussian behavior for large  $K$ . However, such behavior is not consistent across  $K$ 's, as observed instead for original data. Solid lines in **B**, **C**, and **E** are linear least-square fit of the form  $\log y = a \cdot \log x + b$ , where  $x = K$  and  $y = -\ln P_0$ ,  $\text{Var}(K)$  and  $\tau_c$ , respectively. Solid line in **F** is a least squares fit to  $\log \lambda = \log b(\text{rank}/K)^{-\mu}$  performed for  $K = 128$ . Results are averaged over 100 realizations of the random pairing. For each quantity, fits are performed on the average. Error bars and shaded areas represent SEM calculated of 100 realizations of the random coarse-graining. Where not shown (the variance and  $P_0$ ), error bars are smaller than the symbol size.

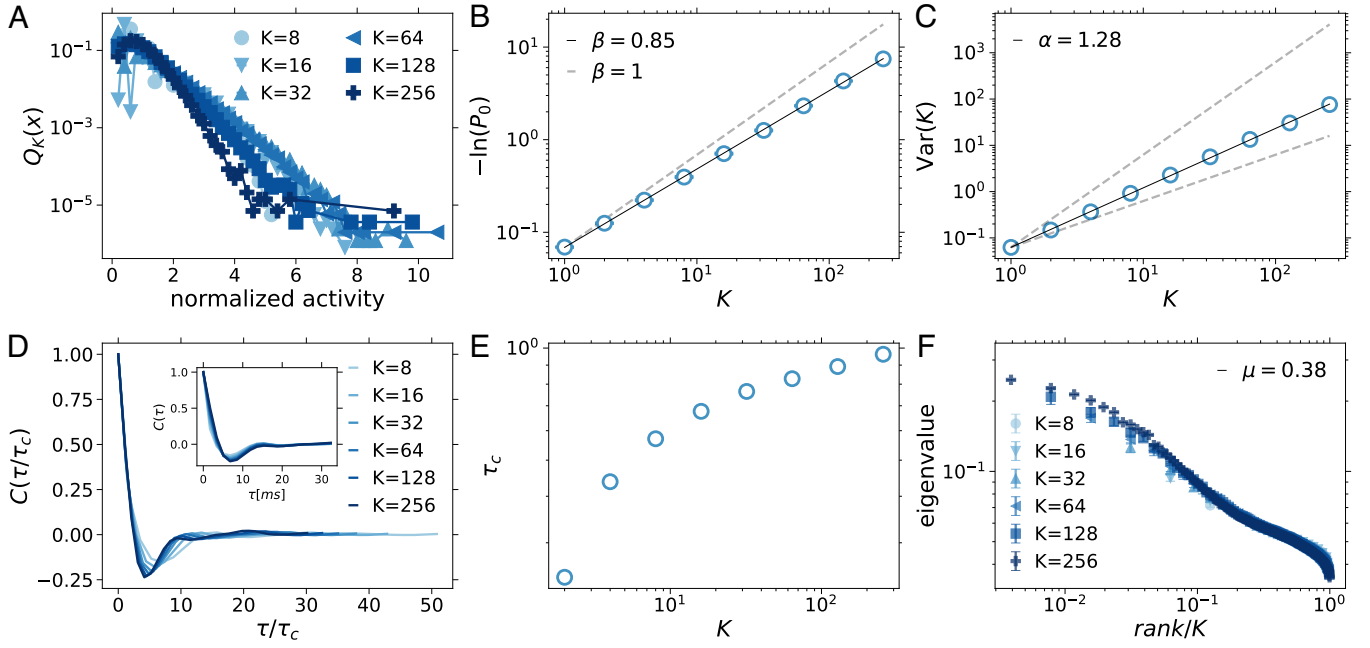


Fig. S10. **PRG analysis performed using a binarization threshold  $e = 0.5\text{SD}$ .** The distribution of cluster activity tends to a Gaussian for increasing cluster sizes (A), while the scaling exponent  $\beta$  slightly increases (B) and  $\alpha$  slightly decreases (C) compared to the values obtained for  $e = 3 \text{ SD}$ . The autocorrelation instead shows no scaling across  $K$  D-E. Scaling and data collapse of the eigenspectra of the cluster covariance matrices are also altered compared to higher binarization thresholds (F). Error bars (SEM) are smaller than symbol sizes (B and F).

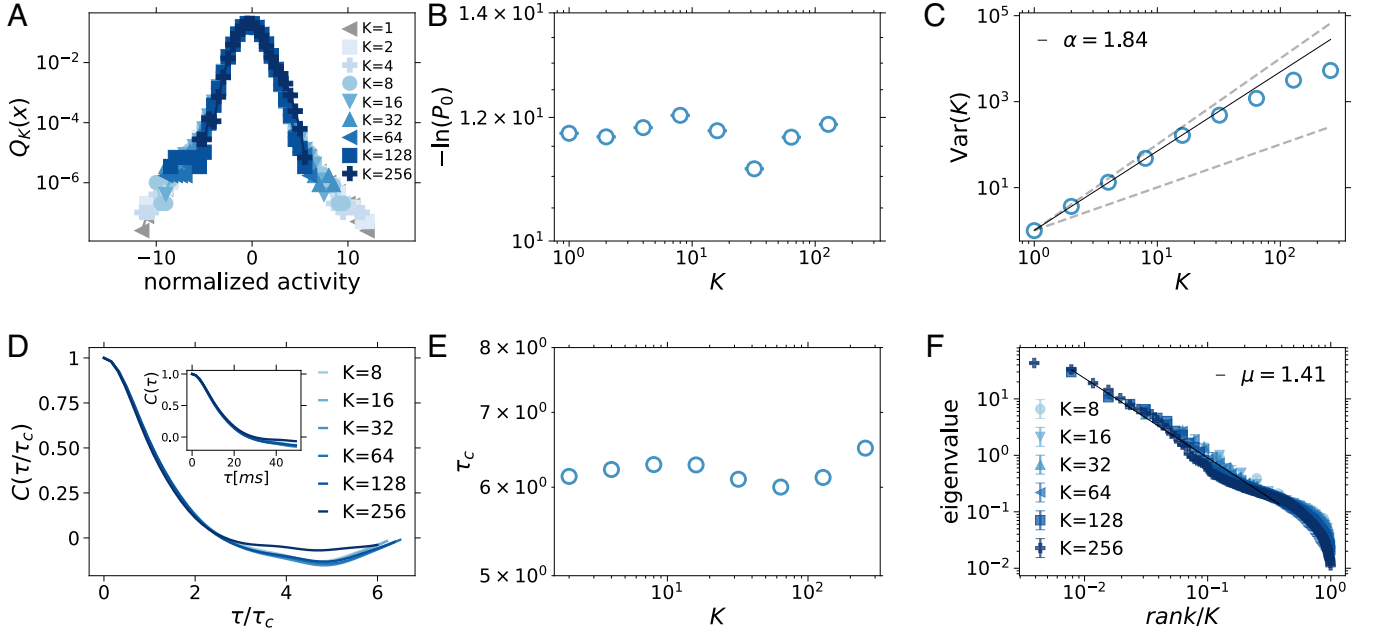


Fig. S11. **PRG analysis performed on continuous MEG data (individual subject).** The probability of activity (A), which initially deviates from a Gaussian for large activity values, progressively approaches a Gaussian form ( $K = 256$ ) that corresponds to the Gaussian core of the original signal amplitude distribution ( $K = 1$ , gray triangles). The probability of silence is independent of  $K$  (B), while the variance (C) scales with an exponent ( $\alpha = 1.84$ ; linear least-square fit of the form  $\log \text{Var}(K) = a \cdot \log K + b$ ) closer to 2 (fully correlated variables, upper dashed line). The autocorrelation of cluster activity is nearly independent of the cluster size  $K$  (D-E). Eigenspectra of the covariance matrix do not show a clear scaling regime and data collapse (F). The solid black line is a least squares fit to  $\log \lambda = \log b(\text{rank}/K)^{-\mu}$  performed for  $K = 128$  (fitting range is  $2/128 - 50/128$ ) and is shown only as a reference and for comparison with Fig. 1 (main text). Values of original MEG signals and coarse-grained variables lower than  $10^{-5}$  were set equal to zero to ensure that  $P_0 \neq 0$  throughout all coarse-graining steps  $P_0 = 0$  in  $K = 256$ . This does not affect results for the other analyzed quantities, which show the same behavior for original data and coarse-grained variables with no zeros. Scaling of  $P_0$  and all other quantities remain stable on a broad range of zero-defining threshold ( $< 0.1$ ). Error bars (SEM) are smaller than symbol size (B and F). Z-normalization is applied to the summed continuous signals at each PRG step. Variance is calculated on the non-normalized variables.

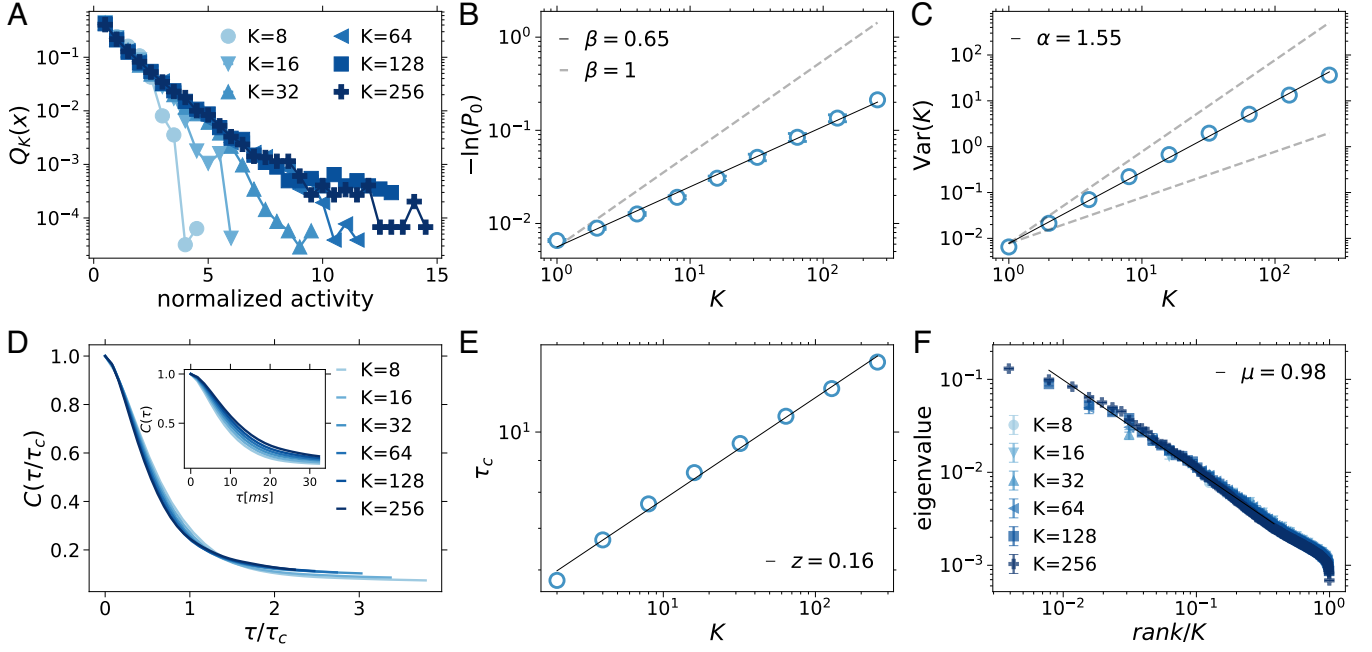


Fig. S12. **PRG analysis performed considering all points of signal excursions above and below thresholds for an individual subject.** As for the case in which one considers only the tip of the excursions (Appendix D), the distribution of activity approaches a universal non-Gaussian form for increasing  $K$  (A). Scaling of silence and variance remains non-trivial (B-C).  $\beta$  decreases and  $\alpha$  increases compared to the values measured when considering only the extremes of the excursions (see Table II). The decay of the variable autocorrelation is slower for increasing  $K$ , and all autocorrelation  $C(\tau)$  collapse on the same curve when  $\tau$  is rescaled by the autocorrelation time  $\tau_c(K)$  (D).  $\tau_c$  scales as  $K^z$ , with  $z = 0.16 \pm 0.03$  (mean  $\pm$  SD;  $n = 100$  subjects) (E). Eigenvalues of cluster covariance matrices decay as a power-law of their scaled ranks ( $\text{rank}/K$ ), with an exponent  $\mu = 0.94 \pm 0.05$  ( $n = 100$  subjects; Table II). The solid line is a least squares fit to  $\log \lambda = \log b(\text{rank}/K)^{-\mu}$  performed for  $K = 128$ . The fitting range is  $2/128 - 50/128$ . Error bars (SEM) are smaller than symbol size (B and F).

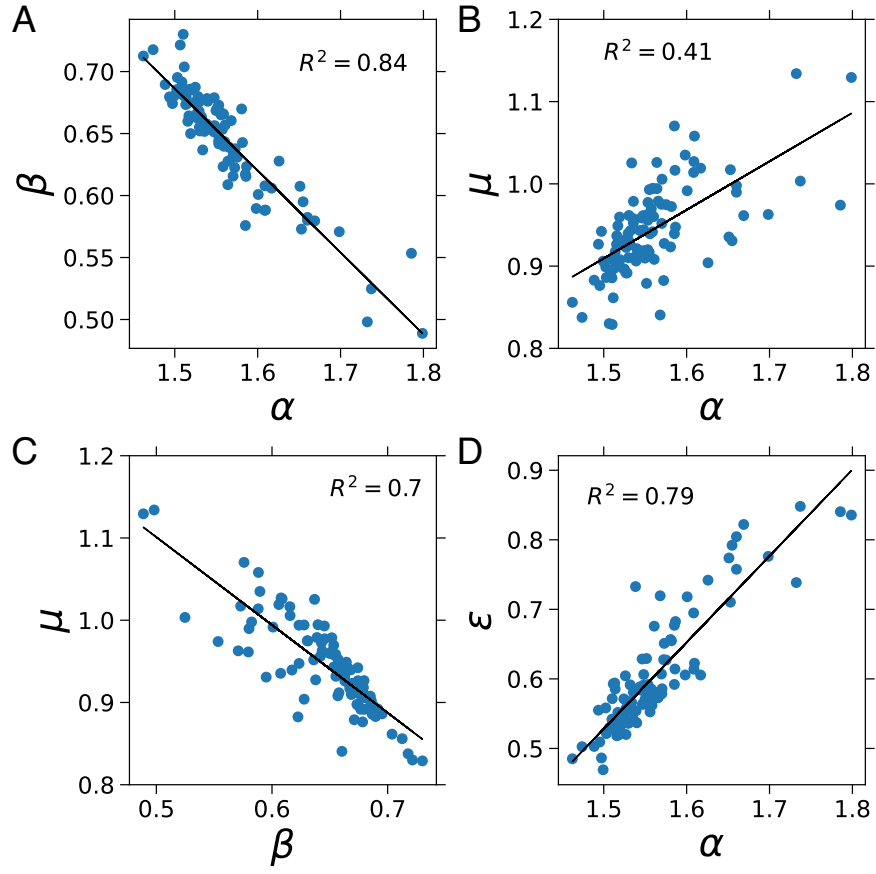


Fig. S13. **Relationships between scaling exponents in the MEG of the resting state considering all points of above and below-threshold excursions.** **A.** The scaling exponent of the cluster variance is inversely proportional to the exponent  $\beta$  that characterizes the the probability of silence  $P_0(K)$ , i.e.  $\beta = -0.66\alpha + 1.68$  (linear least square fit;  $R^2 = 0.84$ ). **B.** The exponent  $\mu$  characterizing the eigenvalue spectrum of the covariance matrix increases linearly with  $\alpha$ :  $\mu = 0.59\alpha + 0.02$  (linear least square fit;  $R^2 = 0.41$ ). **C.** As expected from A and B, the exponent  $\mu$  decreases for increasing values of  $\beta$ . The relationship between  $\mu$  and  $\beta$  is well described by a linear equation,  $\mu = -1.07\beta + 1.63$  (linear least square fit;  $R^2 = 0.7$ ). **D.** The scaling exponent of the largest eigenvalue of the covariance matrix,  $\epsilon$ , increases for increasing values of  $\alpha$ , as shown by the linear relationship  $\epsilon = 1.24\alpha - 1.34$  (linear least square fit;  $R^2 = 0.79$ ).

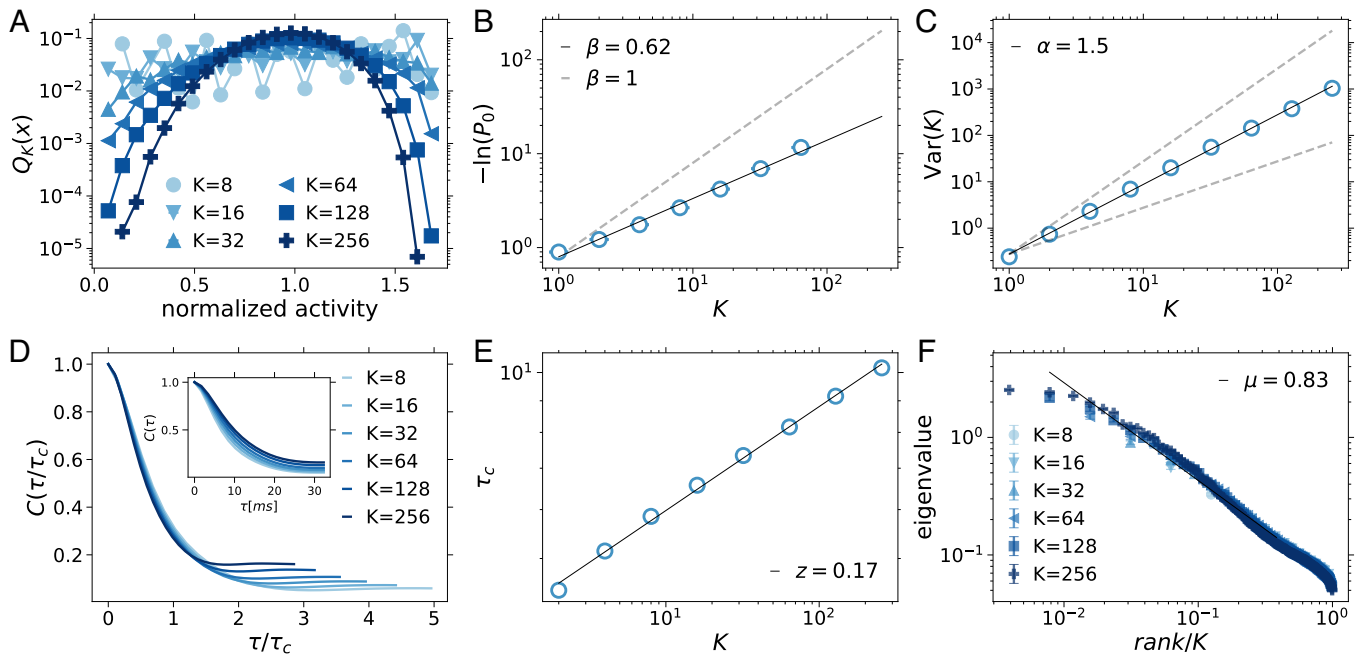


Fig. S14. PRG analysis performed using a binarization threshold  $e = 0.5$  SD and considering all points belonging to beyond-threshold excursions. Scaling is comparable to the one observed for  $e = 3$  SD for all quantities (Fig. S12). Error bars (SEM) are smaller than symbol size (B and F).

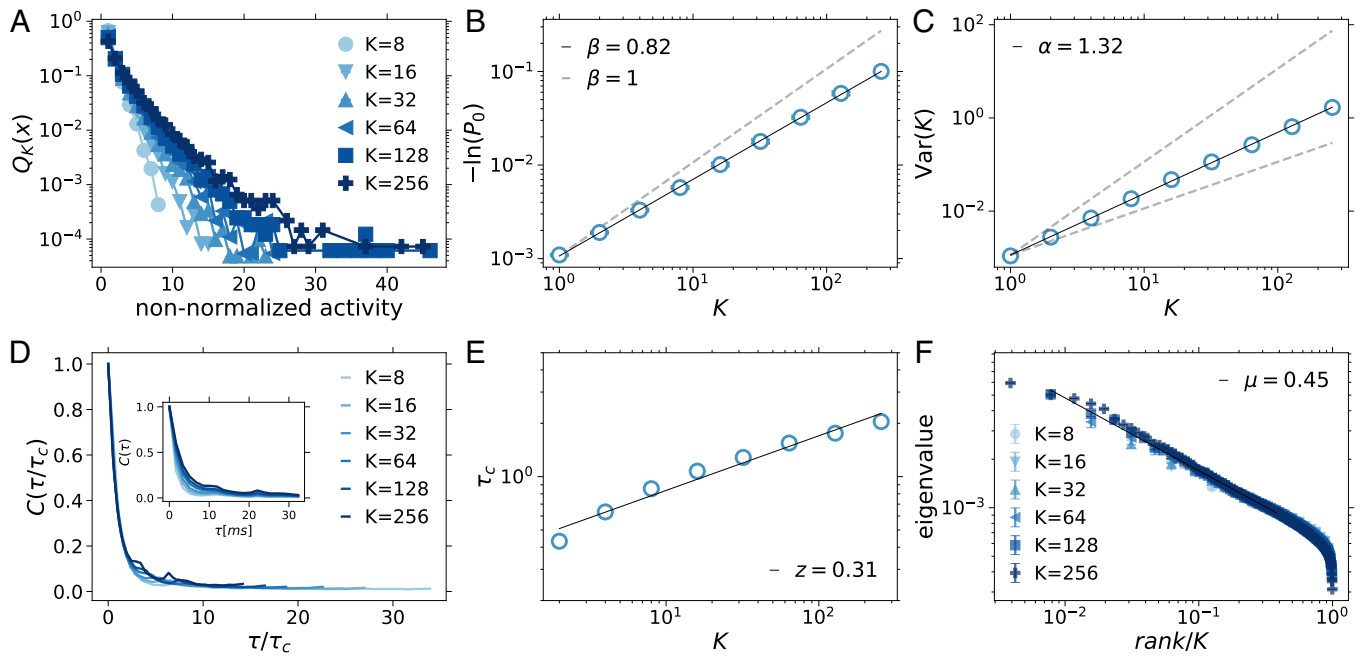


Fig. S15. **PRG analysis performed on non-normalized variables for an individual subject.** For all analyzed quantities, results of the PRG analysis performed on non-normalized variables are in line with those obtained from normalized variables (Fig. 1, main text, individual subject; Fig. S1, average over subjects). Error bars (SEM) are smaller than symbol size (B and F).

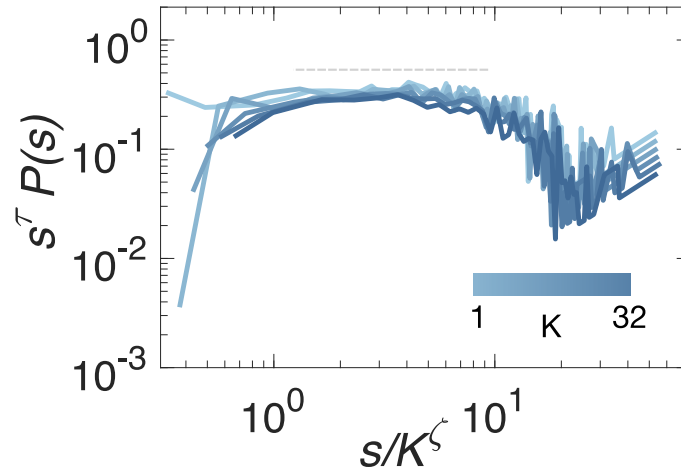


Fig. S16. **Scaling regime of avalanche size distributions is approximately invariant under coarse-graining.** Distributions of avalanche sizes for different cluster sizes  $K$  approximately collapse onto a single curve for  $\tau = 1.3$  and  $\zeta = 0.2$ . The exponent  $\tau$  obtained from the data collapse is slightly smaller than the value obtained from maximum likelihood estimates over the entire range of avalanche sizes. The analysis was performed on the individual subject used for Fig. 2 and 4 of the main text. Results are consistent across subjects.

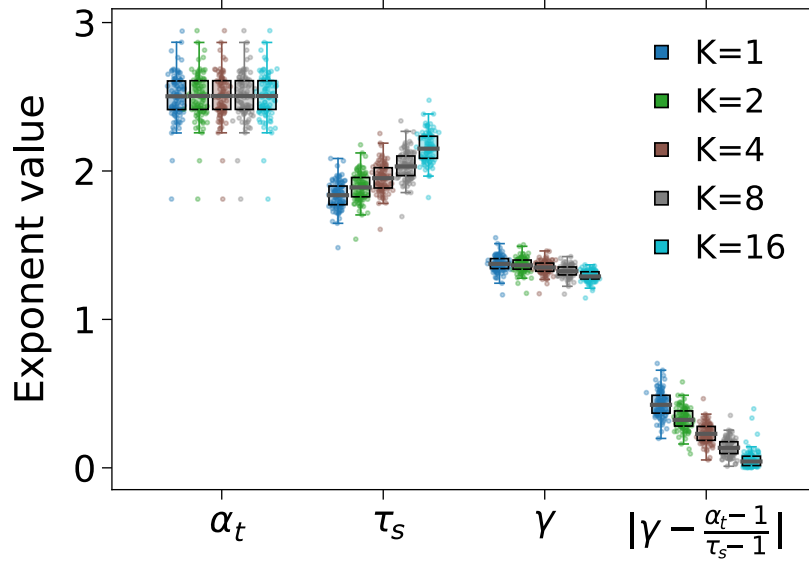


Fig. S17. **Exponents  $\tau_s$ ,  $\alpha_t$ ,  $\gamma$  and corresponding scaling relationship for neuronal avalanches during coarse-graining.** The exponent  $\tau_s$  of the avalanche size distribution slightly increased for increasing cluster sizes,  $K = 1, 2, 4, 8, 16$ :  $1.83 \pm 0.09$ ,  $1.89 \pm 0.10$ ,  $1.95 \pm 0.10$ ,  $2.03 \pm 0.10$ ,  $2.16 \pm 0.10$  (*mean  $\pm$  SD*). The exponent  $\alpha_t$  of the avalanche duration distribution remained unchanged across  $K$ :  $\alpha_t = 2.50 \pm 0.16$  (*mean  $\pm$  SD*). The exponent  $\gamma$  slightly decreases for increasing  $K = 1, 2, 4, 8, 16$ :  $1.37 \pm 0.05$ ,  $1.36 \pm 0.05$ ,  $1.35 \pm 0.04$ ,  $1.32 \pm 0.04$ ,  $1.29 \pm 0.04$  (*mean  $\pm$  SD*). The difference  $|\frac{\alpha_t - 1}{\tau_s - 1} - \gamma|$  tends to zero for increasing  $K$ , suggesting that the system is getting closer to criticality. From  $K = 1$  to  $K = 16$ , the difference is:  $0.43 \pm 0.09$ ,  $0.33 \pm 0.08$ ,  $0.23 \pm 0.07$ ,  $0.14 \pm 0.06$ ,  $0.06 \pm 0.06$  (*mean  $\pm$  SD*). Maximum likelihood estimates were performed following [59] using the range between  $T_{min} = S_{min} = 1$  and  $T_{max} = max(T)$ ,  $S_{max} = 1.5N_k$ . Black box and line: interquartile range (IQR),  $Q_3 - Q_1$ . and median. Whiskers: 1.5 IQR.

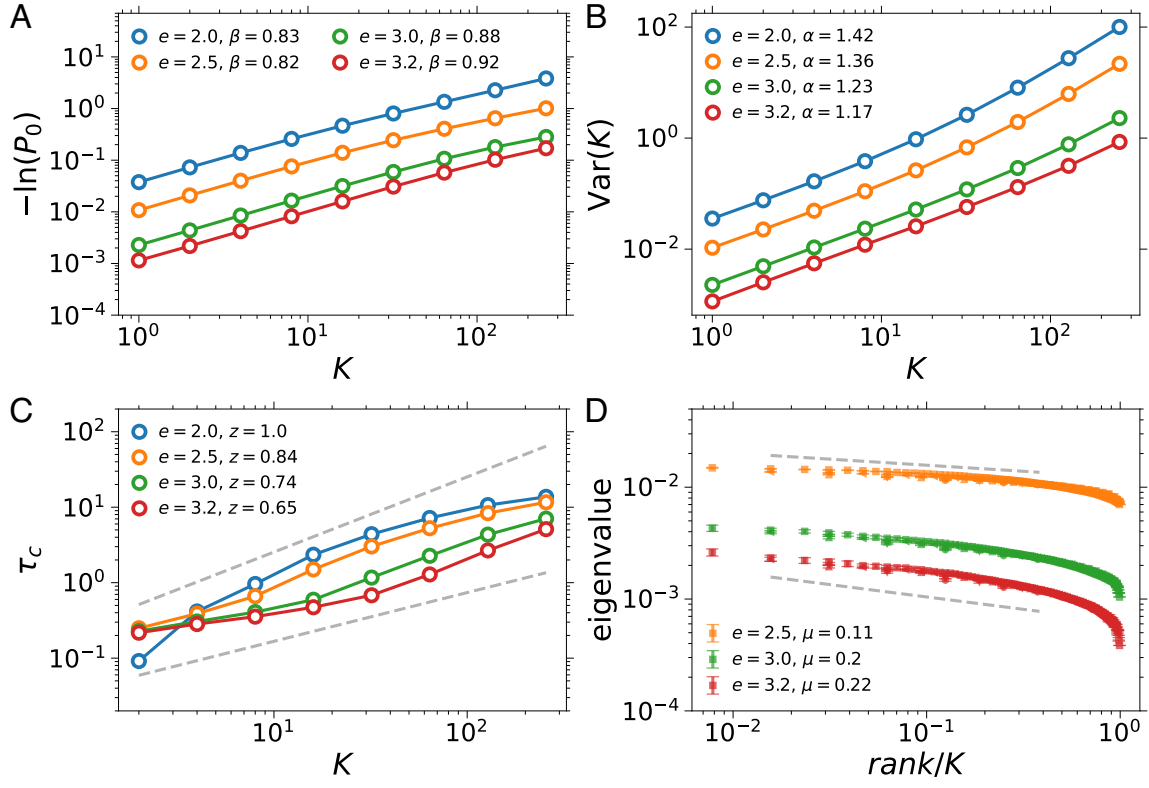


Fig. S18. **Robustness of scaling behaviors with respect to binarization threshold in model simulations. A.** Distributions of silence robustly follow the functional form  $P_0 = e^{-aK^\beta}$  for a range of binarization threshold,  $2.0 \leq e \leq 3.2$  SD. The exponent  $\beta$  shows small variability for  $e \leq 3.2$  SD, increasing for  $e > 3$  SD. This is expected since more and more points are removed from the timeseries as one increases the threshold. **B.** The variance scaling  $Var(K)$  remains robust across binarization thresholds. For  $e > 3$  SD the exponent tends to 1, the prediction for independent variables. **C.** Autocorrelation time,  $\tau_c$ , as a function of  $K$ . Scaling exponent decreases with increasing  $e$ , and show little variability in a range around  $e = 3$  SD, the value used for empirical and model data analysis in Figs. 2, 5 and 6. Fit is performed between  $K = 2$  and  $K = 256$ . Dashed lines represent the fit for  $e = 2$  and  $e = 3.2$  SD. **D.** Dependence of eigenvalue spectra on the threshold  $e$ . Dashed lines represent the fit for  $e = 2.5$  and  $e = 3.2$  SD. The analysis is performed using  $\delta = 1dt$ .

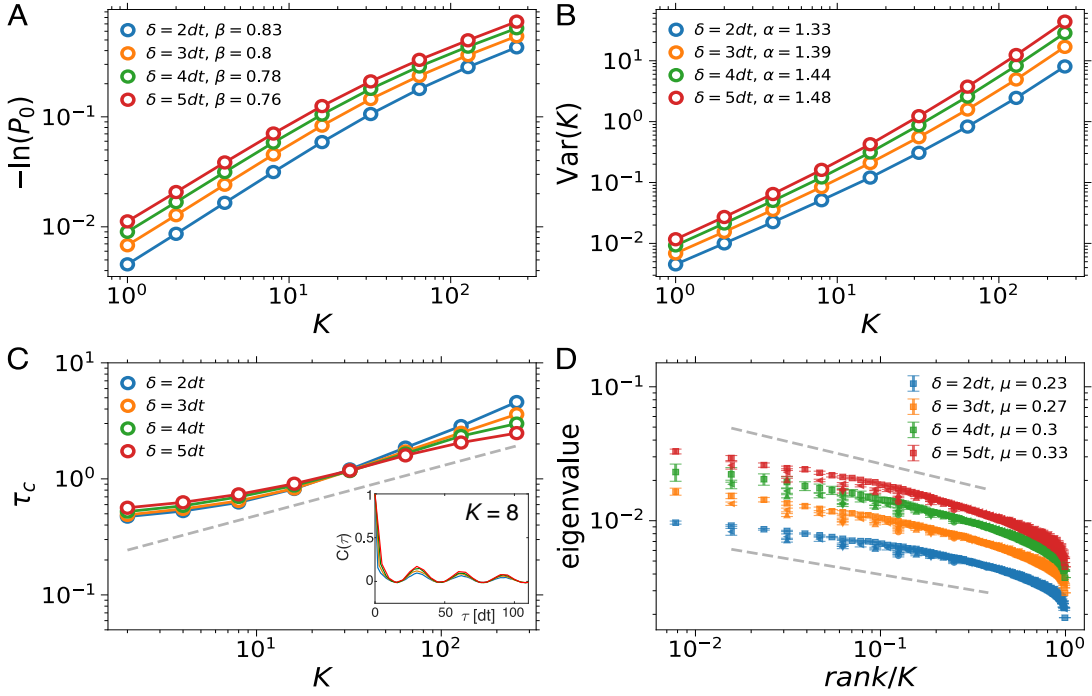


Fig. S19. **Dependence of scaling behaviors of the model on temporal binning.** **A.** Distributions of silence follow the equation  $P_0 = e^{-aK^\beta}$  in the range of time bin sizes, from  $2dt$  to  $5dt$ , where  $dt$  is the simulation timestep corresponding to one system sweep. The exponent  $\beta$  tends to decrease for increasing bin sizes, and goes from  $0.83$  at  $\delta = 2dt$  to  $\beta = 0.76$  at  $\delta = 5dt$ . **B.** The scaling exponent of the variance,  $\alpha$ , increases with the bin size  $\delta$ . Although rather limited, this increase indicates that binning increases correlations among variables. **C.** Autocorrelation time,  $\tau_c$ , as a function of  $K$ .  $\tau_c(K)$  is in unit of  $\delta$ . The approximate data collapse of curves corresponding to different  $\delta$  shows that the relationship between  $\tau_c$  and  $K$  is weakly dependent on time binning, except for the largest cluster  $K = 256$ . Inset: Representative  $C(\tau)$  for different  $\delta$  and  $K = 8$ . **D.** The scaling behavior and the corresponding exponent of the eigenvalue spectrum show little dependence on the choice of time binning. The exponent  $\mu$  slightly increases with  $\delta$ . Dashed lines represent the fit for  $\delta = 2dt$  and  $\delta = 5dt$ . All quantities are calculated for a simulation of a network with  $N = 273000$  and  $M = 273$  subsystems made of  $n_{sub} = 1000$  neurons. The threshold used is  $e = 3$  SD.

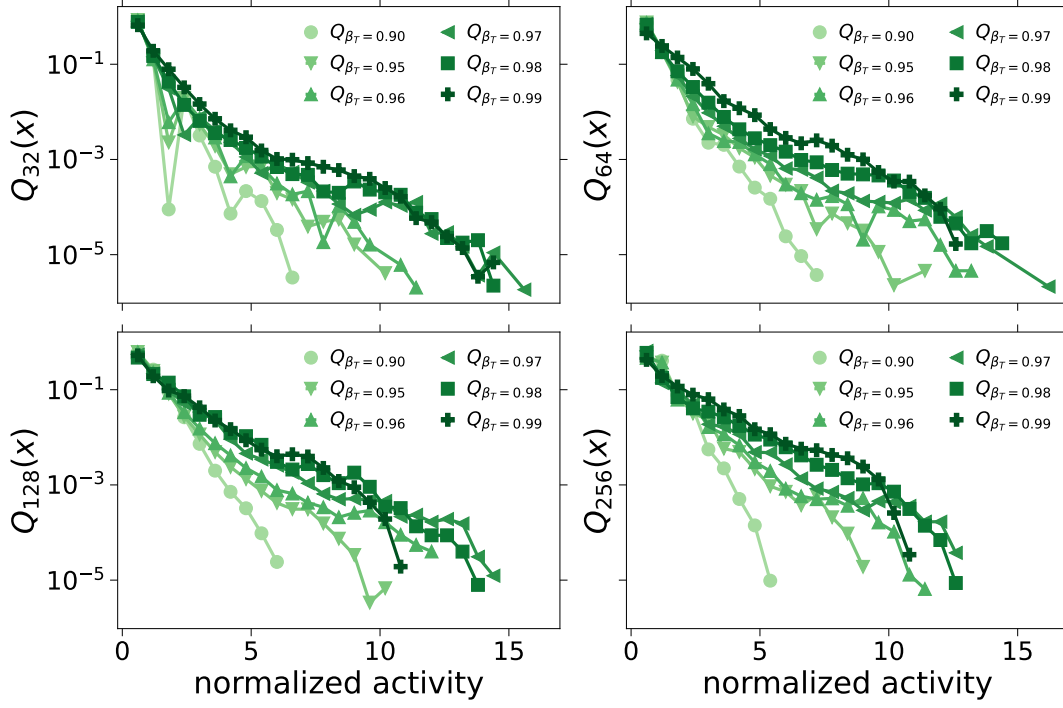


Fig. S20. **Effect of the distance from criticality  $DTC = \beta_c - \beta_T$  on the distribution of activity for  $K = 32, 64, 128, 256$ .** For  $DTC > 0.05$  ( $\beta_T < 0.95$ ) the distributions are short-tailed and approximately Gaussian for all  $K$ . As  $\beta_T$  approaches the critical point the distributions become distinctly non-Gaussian. Simulation of a network with  $N = 273000$  and  $M = 273$  subsystems made of  $n_{sub} = 1000$  neurons. The threshold and bin size used are  $e = 3$  SD and  $\delta = 3dt$ .

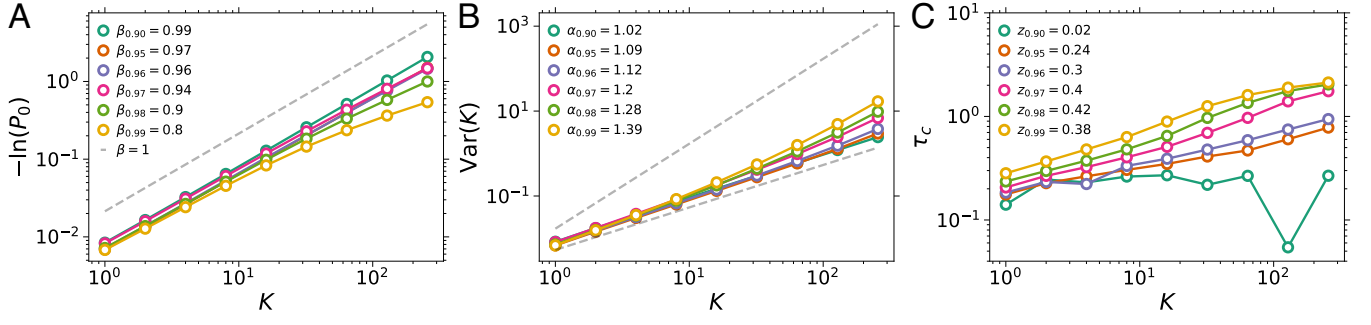


Fig. S21. **Scaling exponents  $\beta$ ,  $\alpha$ , and  $z$  as a function of  $DTC = \beta_c - \beta_T$ .** **A.** For  $P_0$ , subcritical values of  $\beta_T < 0.98$  ( $DTC > 0.02$ ) the exponent  $\beta$  controlling the scaling of  $P_0(K)$  tends to 1, the value expected for independent, random variables ( $\beta \approx 1$ ). **B.** Non-trivial scaling emerges very close to the critical point, for  $DTC \leq 0.03$  ( $\beta_T \geq 0.97$ ). **C.** Scaling in the autocorrelation time,  $\tau_c$ , is progressively lost for  $DTC > 0.05$  ( $\beta_T < 0.95$ ). Simulation of a network with  $N = 273000$  and  $M = 273$  subsystems made of  $n_{sub} = 1000$  neurons. The threshold and bin size used are  $e = 3$  SD and  $\delta = 3dt$ .

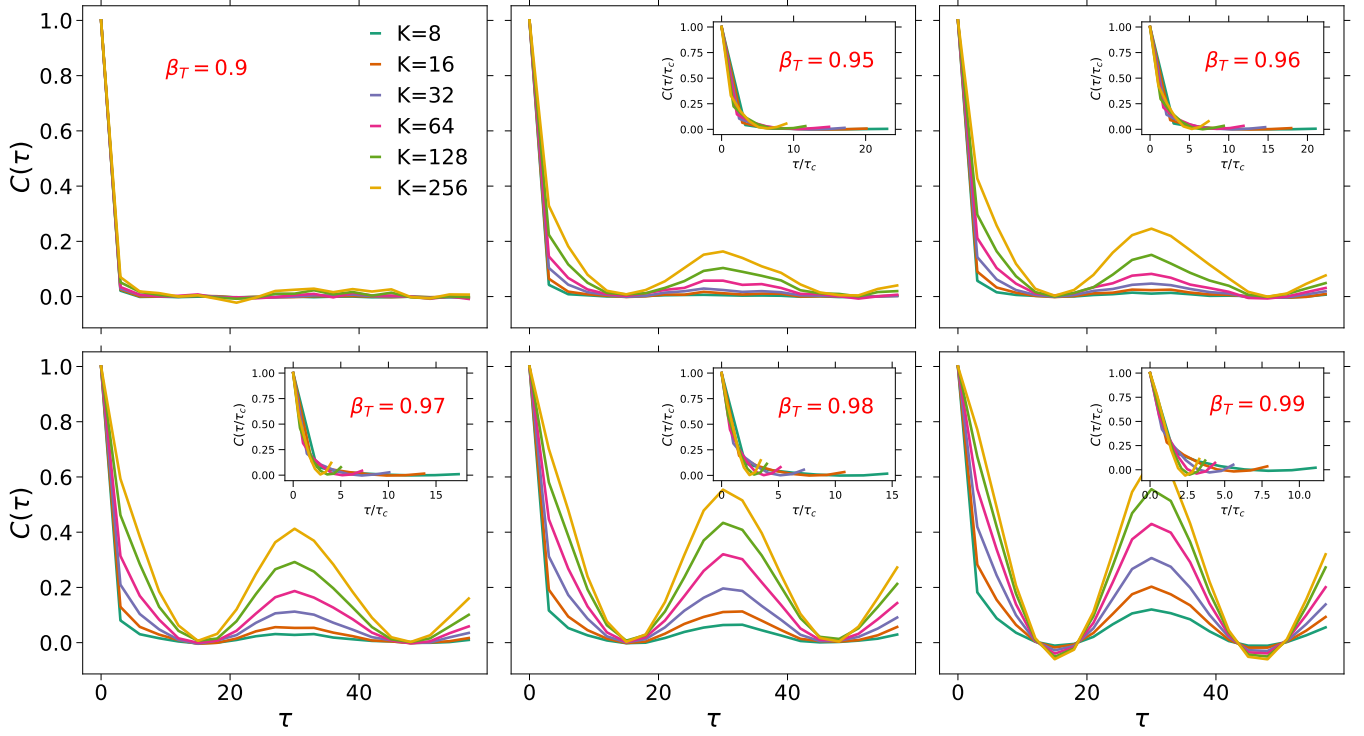


Fig. S22. **Effect of the distance from criticality  $DTC = \beta_c - \beta_T$  on the autocorrelation of cluster activity.** Average autocorrelation for different cluster sizes ( $K$ ) and  $\beta_T$  values (main panels). For  $\beta_T < 0.95$ , i.e.  $DTC > 0.05$  the autocorrelation is independent of  $K$ , indicating no scaling of  $\tau_c$ . Moreover, oscillations characteristic of large  $K$ 's progressively fade out as we move away from the critical point. Insets: Autocorrelation as a function of rescaled time,  $\tau/\tau_c$ . Data collapse onto a single curve for  $\beta_T \geq 0.95$  ( $DTC \leq 0.05$ ).

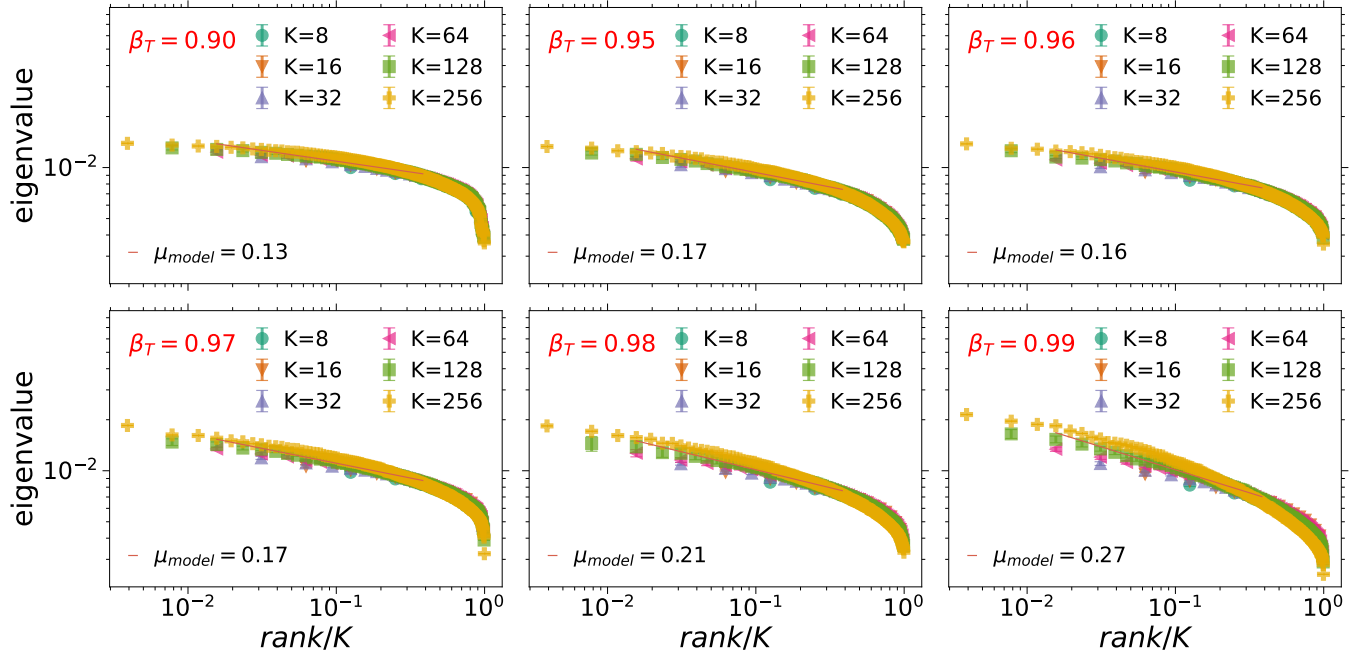


Fig. S23. **Effect of the distance to criticality  $DTC = \beta_c - \beta_T$  on the scaling of the eigenspectrum of the covariance matrix.** Scaling is preserved for  $DTC \leq 0.03$  ( $\beta_T \geq 0.97$ ) and progressively lost for higher  $DTC$  values ( $\beta_T \leq 0.96$ ).

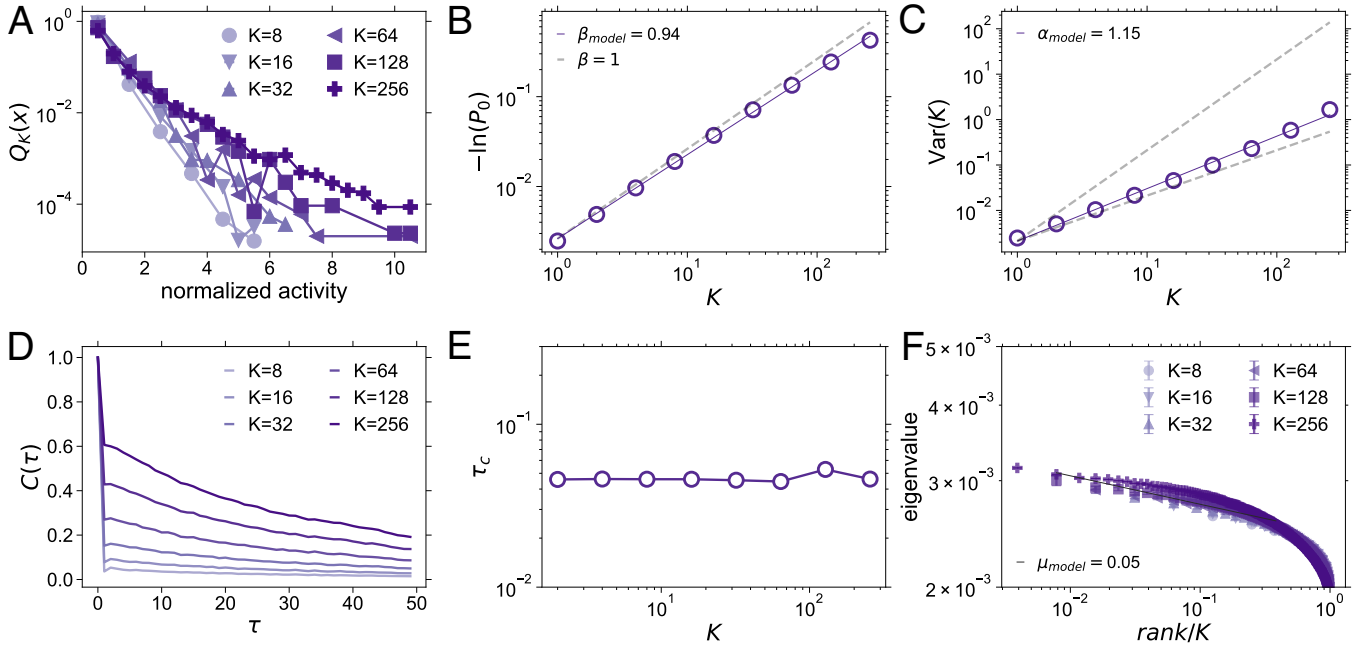


Fig. S24. **PRG in the fully connected adaptive Ising model without feedback shows (mostly) trivial scaling.** **A.** Probability distribution of normalized non-zero activity for cluster sizes  $K \geq 8$ . Darker shades of red correspond to increasing cluster sizes. **B.** The log-probability of silence in coarse-grained variables ( $-\ln P_0$ ) as a function of cluster size ( $K$ ). The solid red line represents a linear least-squares fit to  $\log(-\ln P_0) = \log K^{\beta_{model}} + b$ , where  $\beta_{model} = 0.94$ , close to the behavior expected for independent variables. **C.** Variance ( $Var$ ) of the coarse-grained variables as a function of cluster size,  $K$ . The solid red line corresponds to the linear least-squares fit,  $\log Var(K) = \alpha \cdot \log K + b$ , where  $\alpha_{model} = 1.15$ , closer to the reference value for independent variables,  $\alpha = 1$ . **D.** Average autocorrelation functions for different cluster sizes ( $K$ ), which lack the oscillatory structure observed in the feedback case. **E.** The autocorrelation time,  $\tau_c$ , is nearly independent of  $K$ , indicating the absence of scaling when feedback is removed.  $\tau_c$  is estimated via non-linear least square fit of the form  $y = A \cdot e^{-\tau/\tau_c} + B \cdot e^{-\tau/\tau_1}$ . **F.** Eigenvalues of cluster covariance matrices for different cluster sizes. Larger clusters correspond to darker colors. In the absence of feedback, the eigenvalue spectrum becomes nearly flat, with a fitted exponent  $\mu_{model} = 0.05$  reflecting loss spectral scaling. Error bars (SEM) are smaller than the symbol size. Simulations were performed near the critical regime ( $\beta = 0.99$ ,  $c = 0.0$ ,  $J = 1$ ) on a network with  $N = 273000$  neurons. The number of sensors was  $M = 273$ , each including  $n_{sub} = 1000$  neurons.

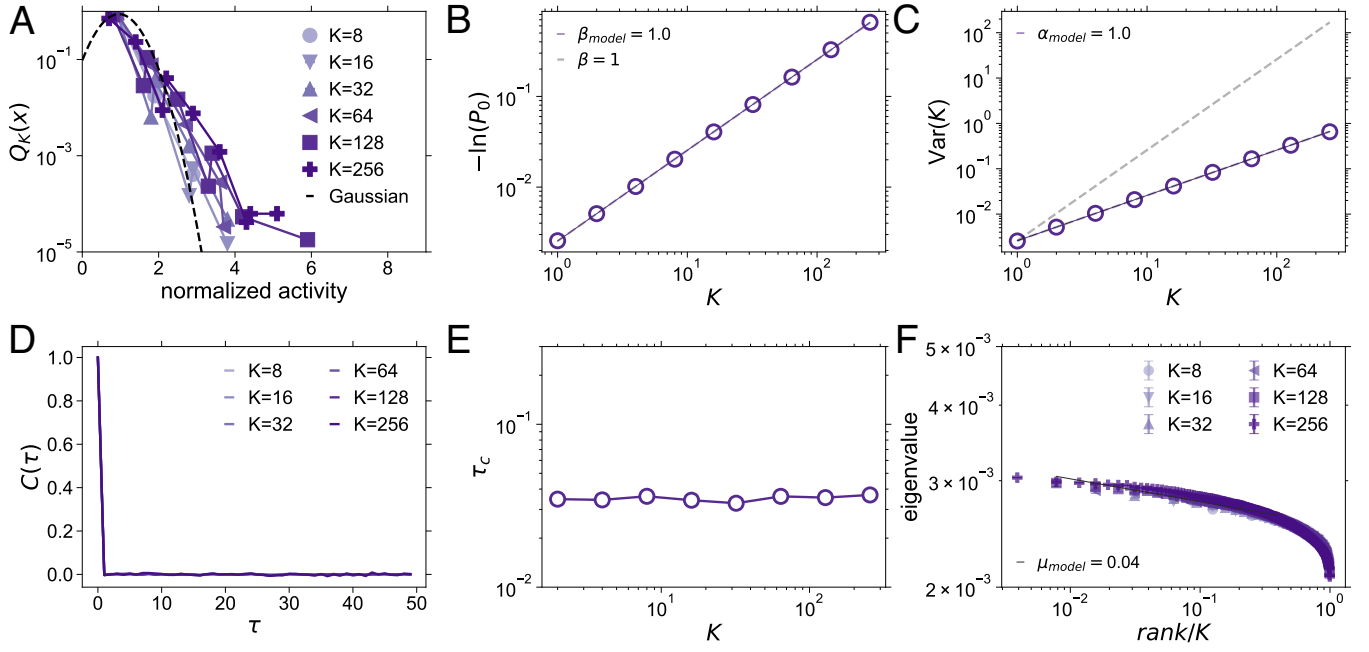


Fig. S25. **PRG in the adaptive Ising model with no synaptic interactions.** **A.** Probability distribution of normalized non-zero activity for cluster sizes  $K \geq 8$ . The distributions are Gaussian, as expected for independent variables. **B.** The log-probability of silence ( $-\ln P_0$ ) as a function of cluster size ( $K$ ). The solid red line represents a linear least-squares fit to  $\log(-\ln P_0) = \log K^{\beta_{model}} + b$ , where  $\beta_{model} = 1$ , the behavior expected for independent variables.  $\beta_{model} = 1$ , fully consistent with the independent-variable prediction. **C.** Variance of coarse-grained variables as a function of cluster size ( $K$ ). A linear least-squares fit of  $\log(\text{Var})$  vs  $\log K$  gives  $\alpha_{model} = 1$ , as expected for independent variables. **D.** Average autocorrelation functions for different cluster sizes ( $K$ ) show absence of correlations. All curves are identical across cluster sizes. **E.** Autocorrelation time ( $\tau_c$ ) as a function of cluster size. Since all clusters have the same autocorrelation function, no scaling in  $\tau_c$  is observed. **F.** Eigenvalues of covariance matrices within clusters for different cluster sizes. The eigenspectra show no scaling. Error bars (SEM) are smaller than the symbol size. Simulations were performed near the critical regime ( $\beta = 0.99$ ,  $c = 0.0$ ), on a network with  $J_{ij} = 0$  and  $N = 273000$  neurons. The number of sensors was  $M = 273$ , each including  $n_{sub} = 1000$  neurons ( $e = 3\text{SD}$ ;  $\delta = 1dt$ ).

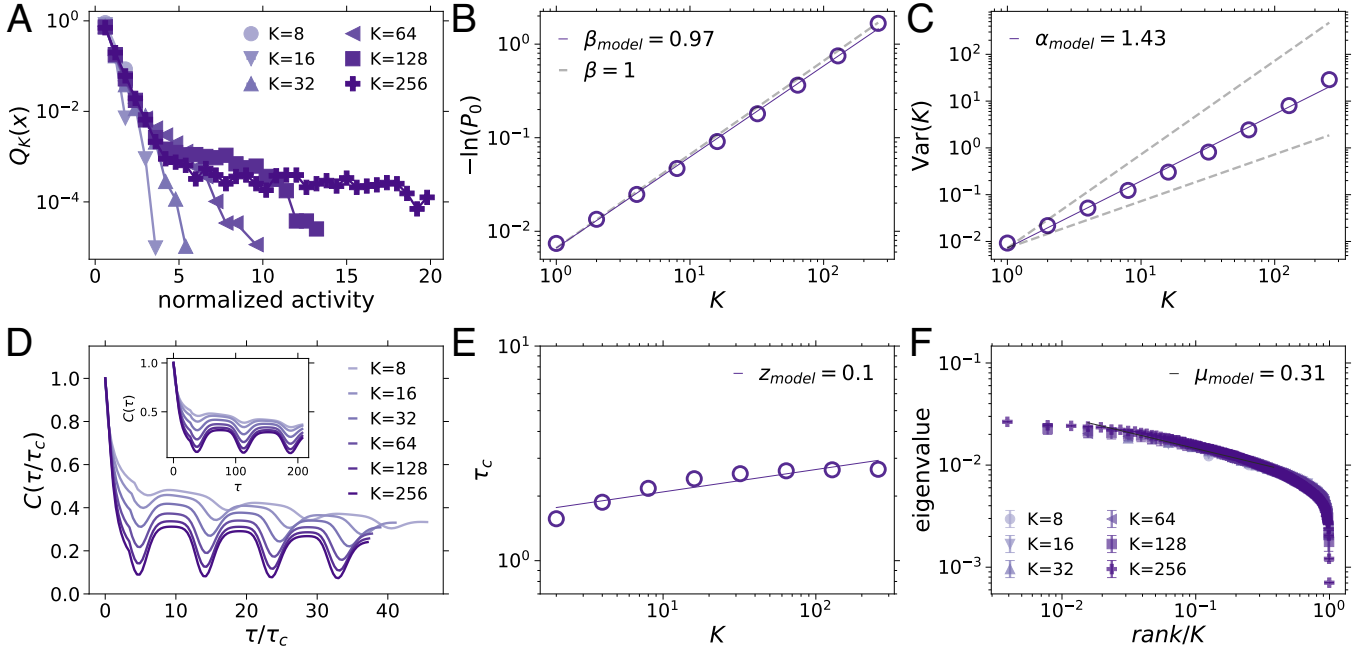


Fig. S26. **PRG analysis of the adaptive Ising model on a 2D network.** **A.** Probability distribution of normalized non-zero activity for cluster sizes  $K \geq 8$ . Darker shades of red correspond to increasing cluster sizes. **B.** The log-probability of silence in coarse-grained variables ( $-\ln P_0$ ) as a function of cluster size ( $K$ ). The solid red line represents a linear least-squares fit to  $\log(-\ln P_0) = \log bK^{\beta_{model}}$ , where  $\beta_{model} = 0.97$ , very close to the behavior expected for independent variables ( $\beta = 1$ ). **C.** Variance ( $\text{Var}$ ) of the coarse-grained variables as a function of cluster size,  $K$ . The solid red line corresponds to the linear least-squares fit,  $\log \text{Var}(K) = \alpha \cdot \log K + b$ , where  $\alpha_{model} = 1.43$ . **D.** Rescaled average autocorrelation functions for different cluster sizes ( $K$ ) collapse in the range of the initial decay exponential decay. The  $C(\tau)$  are smoothed with a 20-points moving average (approximate period of the oscillatory trend).  $\tau_c$  is estimated via non-linear least square fit of the form  $y = A \cdot e^{-\tau/\tau_c} + B \cdot e^{-\tau/\tau_1}$ . Inset: Non-rescaled  $C(\tau)$ . **E.** The autocorrelation time,  $\tau_c$ , scales as a power-law of  $K$ , with an exponent  $z_{model} = 0.12$ . **F.** Eigenvalues of cluster covariance matrices for different cluster sizes. Larger clusters correspond to darker colors. Eigenvalues. The solid line is a least squares fit to  $\log \lambda = \log b(\text{rank}/K)^{-\mu}$  performed for  $K = 128$ . The fitting range is  $[2/128, 50/128]$ . Error bars represent SEM and are smaller than the symbol size. Simulations were performed near the critical regime of the 2D model ( $\beta = 0.43$ ,  $c = 0.01$ ,  $J = 1$ ) on a network with  $N = 256 \cdot 10^5$  neurons. The number of sensors was  $M = 256$ , each including  $n_{sub} = 10^5$  neurons ( $e = 2.5$  SD;  $\delta = 3dt$ ).

## Supplementary Tables

Scaling exponent	Extreme point of positive excursions	Extreme point of negative excursions
$\beta$	$0.83 \pm 0.02$	$0.84 \pm 0.02$
$\alpha$	$1.30 \pm 0.04$	$1.29 \pm 0.03$
$z$	$0.31 \pm 0.04$	$0.30 \pm 0.03$
$\mu$	$0.42 \pm 0.04$	$0.43 \pm 0.04$

TABLE I. **Scaling exponents when considering only positive or only negative extremes of above-threshold excursions.** The threshold is  $e = 3.0SD$ . Errors are standard deviations over 100 subjects.

Scaling exponent	All points in the excursion	Extreme point of excursion only
$\beta$	$0.64 \pm 0.04$	$0.82 \pm 0.02$
$\alpha$	$1.56 \pm 0.06$	$1.32 \pm 0.03$
$z$	$0.16 \pm 0.03$	$0.33 \pm 0.03$
$\mu$	$0.94 \pm 0.05$	$0.41 \pm 0.03$

TABLE II. **Scaling exponents for the two different event detection approaches.** Binarization threshold is  $e = 3.0SD$ . Errors are standard deviations over 100 subjects.

Scaling exponent	All points of positive excursions	All points of negative excursions
$\beta$	$0.66 \pm 0.05$	$0.67 \pm 0.04$
$\alpha$	$1.53 \pm 0.06$	$1.51 \pm 0.05$
$z$	$0.14 \pm 0.03$	$0.13 \pm 0.02$
$\mu$	$0.95 \pm 0.06$	$0.95 \pm 0.06$

TABLE III. **Scaling exponents when considering only positive or only negative above-threshold excursions (all points in the excursions).** The threshold is  $e = 3.0SD$ . Errors are standard deviations over 100 subjects.